GLIA

GLIA 58:1197–1207 (2010)

Glycosphingolipid Synthesis in Cerebellar Purkinje Neurons: Roles in Myelin Formation and Axonal Homeostasis

SHUN WATANABE,[1,2,3] SHOGO ENDO,[4] ERIKO OSHIMA,[1] TOMIKO HOSHI,[5,6] HIDEYOSHI HIGASHI,[3] KAZUYUKI YAMADA,[8] KOUJIRO TOHYAMA,[6] TADASHI YAMASHITA,[7] AND YOSHIO HIRABAYASHI[1,2]*

[1]*Laboratory for Molecular Membrane Neuroscience, Brain Science Institute, RIKEN, Wako-Shi, Saitama, Japan*
[2]*CREST, Japan Science and Technology Agency, Kawaguchi-Shi, Saitama, Japan*
[3]*Division of Glyco-signal Research, Institute of Molecular Biomembrane and Glycobiology, Tohoku Pharmaceutical University, Sendai-Shi, Miyagi, Japan*
[4]*Aging Regulation Team, Tokyo Metropolitan Institute of Gerontology, Itabashi-Ku, Tokyo, Japan*
[5]*Support Unit for Neuromorphological Analysis, Research Resources Center, Brain Science Institute, RIKEN, Wako-Shi, Saitama, Japan*
[6]*The Center for EM and Bio-Imaging Research, Nano-Neuroanatomy, Iwate Medical University, Morioka-Shi, Iwate, Japan*
[7]*Graduate School of Life Science, Hokkaido University, Sapporo-Shi, Hokkaido, Japan*
[8]*Support Unit for Animal Experiment, Research Resources Center, Brain Science Institute, RIKEN, Wako-Shi, Saitama, Japan*

KEY WORDS
glycolipid; glucosylceramide; glycosyltransferase; myelination; Purkinje neuron

ABSTRACT
Glycosphingolipids (GSLs) occur in all mammalian plasma membranes. They are most abundant in neuronal cells and have essential roles in brain development. Glucosylceramide (GlcCer) synthase, which is encoded by the *Ugcg* gene, is the key enzyme driving the synthesis of most neuronal GSLs. Experiments using conditional Nestin-Cre *Ugcg* knockout mice have shown that GSL synthesis *in vivo* is essential, especially for brain maturation. However, the roles of GSL synthesis in mature neurons remain elusive, since Nestin-Cre is expressed in neural precursors as well as in postmitotic neurons. To address this problem, we generated Purkinje cell-specific *Ugcg* knockout mice using mice that express Cre under the control of the L7 promoter. In these mice, Purkinje cells survived for at least 10–18 weeks after *Ugcg* deletion. We observed apparent axonal degeneration characterized by the accumulation of axonal transport cargos and aberrant membrane structures. Dendrites, however, were not affected. In addition, loss of GSLs disrupted myelin sheaths, which were characterized by detached paranodal loops. Notably, we observed doubly myelinated axons enveloped by an additional concentric myelin sheath around the original sheath. Our data show that axonal GlcCer-based GSLs are essential for axonal homeostasis and correct myelin sheath formation.

INTRODUCTION

Glycosphingolipids (GSLs) form lipid microdomains (rafts) that serve as key assembly and sorting platforms for cell–cell interactions and signal transduction complexes. They are also involved in the regulation of multiple cellular processes. Glucosylceramide (GlcCer) is the core precursor molecule of most GSLs, which have many different carbohydrate chains. Some GSLs (e.g., gangliosides) even contain sialic acids. GlcCer synthesis is catalyzed by glucosyltransferase, which is encoded by the *Ugcg* gene (Ichikawa and Hirabayashi, 1998). In addition, a few GSLs that are characteristic components in myelin are derived from galactosylceramide.

Previous studies have suggested that GSLs play an important role in neural cells for processes such as axonal elongation (Boldin and Futerman, 1997; Mutoh et al., 1998; Schwarz and Futerman 1997); synaptic transmission (Fujii et al., 2002); and neuron-glia interactions (Vyas et al., 2002). To elucidate their physiological functions *in vivo*, researchers have generated ganglioside synthase gene knockout (KO) mice. Disruption of the mouse *Ugcg* gene results in embryonic lethality during gastrulation, demonstrating an essential role of the *Ugcg* gene in embryo survival (Yamashita et al., 1999). Mice lacking complex gangliosides reach adulthood with nervous system deficits (Inoue et al., 2002; Sheikh et al., 1999; Sugiura et al., 2005; Yamashita et al., 2005b). Jennmann et al. (2005) also generated neural cell-specific disruption of the *Ugcg* gene using a Nestin-Cre transgenic deleter strain. These mice displayed neuronal defects and died between postnatal Days 11 and 24, suggesting that GSLs are required for brain maturation after birth. Compared with mice lacking complex gangliosides, Jennmann et al.'s *Ugcg* knockout mice have a severe phenotype, emphasizing the importance of GlcCer-based GSLs in the nervous system. However, because GSL synthesis was suppressed in both neuronal and non-neuronal cells, such as radial glia, it is unclear

Additional Supporting Information may be found in the online version of this article.

Grant sponsors: Grant-in-Aid for Strategic Medical Science Research Center, Ministry of Education, Culture, Sports, Science and Technology of Japan, 2009-2013; CREST of JST (Japan Science and Technology Agency).

*Correspondence to: Yoshio Hirabayashi, Laboratory for Molecular Membrane Neuroscience, Brain Science Institute, RIKEN, 2-1 Hirosawa, Wako-shi, Saitama 351-0198, Japan. E-mail: hirabaya@riken.jp

Received 16 October 2009; Accepted 10 March 2010

DOI 10.1002/glia.20999

Published online 9 April 2010 in Wiley InterScience (www.interscience.wiley.com).

whether the observed axonal dystrophy and neurodegeneration represented neuron-autonomous defects. Since neighboring non-neuronal cells such as astrocytes and oligodendrocytes support neuronal cell survival and function, glial-expressed GSLs might influence neurons indirectly, via neuronal-glial interactions; for example, GSLs on astrocytes can affect axonal elongation (Freire et al., 2004). In addition, the short survival time of Nestin-Cre-driven conditional *Ugcg* KO mice precludes the examination of GlcCer-based GSL function at adult stages.

In this study, we generated Purkinje cell-specific *Ugcg* KO mice by crossing L7 gene promoter-driven *Cre* transgenic mice and *Ugcg*-flanked mice. In the cerebellum of *L7-Cre* : $Ugcg^{loxP/loxP}$ mice, Cre expression was specific to Purkinje cells three weeks after birth, when most Purkinje cells have already matured. We observed dystrophic morphology of Purkinje cell axons and subsequent degeneration. Furthermore, our histological analyses demonstrated that axonal transport cargos abnormally accumulated in swollen axons, suggesting that axonal transport was impaired in *Ugcg* (−/−) neurons. These mice displayed an unusual myelin morphology in which some axons were "doubly myelinated," having what appeared to be an additional compact myelin sheath completely enveloping the original myelin sheath. Our results suggested that *de novo* synthesis of GSLs in neurons is essential for the maintenance of axonal homeostasis and normal myelin formation.

MATERIALS AND METHODS

Transgenic Animals

Mice with loxP-flanked exons 7-9 of the *Ugcg* gene locus were generated as described (Yamashita et al., 2005a). For the generation of mice with a Purkinje cell-specific deletion of *Ugcg*, homozygous floxed mice were crossed with homozygous *L7-Cre* mice to generate double-heterozygous offspring. These were intercrossed to yield $Ugcg^{loxP/+}$: $L7\text{-}Cre^{tg/tg}$ mice, which were finally crossed with $Ugcg^{loxP/loxP}$ mice to yield $Ugcg^{loxP/loxP}$: $L7\text{-}Cre^{tg/0}$ mice for analysis (Fig. 1A). These mice appeared in the expected Mendelian ratio of around 50% of the litters. Their $Ugcg^{loxP/+}$: $L7\text{-}Cre^{tg/0}$ littermates were used as controls in each experiment.

Genotyping of Mutant Mice

PCR analysis of tail biopsies was performed for confirmation of the wild-type, floxed, and null alleles (Fig. 1A). For PCR, the following primers were used: Ugcg/wild type forward (primer 1; Fig. 1A), 5′-ATGTGCTAGATCAGGCA GGAGGGCTCATAG-3′; wild type/Ugcg-flox reversed (primer 2), 5′-CCAACAGATATTGAATGCGAATGCTCTG CC-3′; Ugcg null reversed (primer 3), 5′-GAGCCAGTCC ATTACTCTCGTTGATTGCAT-3′. PCR products of about 230 bp, 280 bp, and 300 bp were indicative of the wild-type, floxed, and null alleles, respectively (Yamashita et al., 2005a). The constitutive L7Cre transgene was detected using the following primers: L7Cre forward, 5′-AGGTTCGTTCACTCATGGA-3′; and L7Cre reverse, 5′-TCGACCAGTTTAGTTACCC-3′. A 200 bp PCR product was indicative of the L7Cre transgene.

Immunohistochemistry and Fluorescent Light Microscopy

Adult mice were anesthetized with 0.1 mL of 50 mg/mL Nembutal. They were perfusion-fixed with 4% (w/v) paraformaldehyde (PFA) in 0.1 M phosphate buffer, pH 7.4,

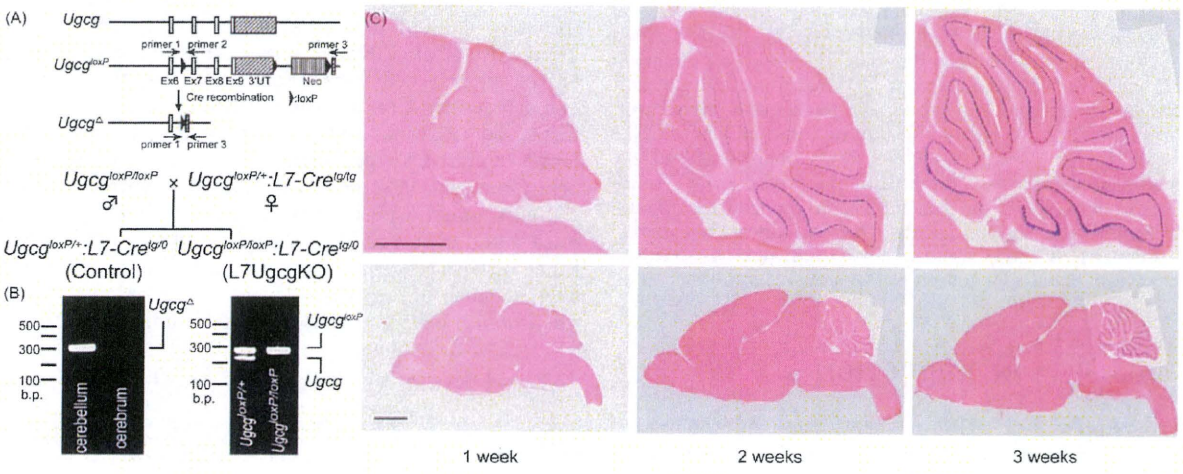

Fig. 1. Generation and characterization of floxed allele. **A**: Schematic representation of Cre-mediated recombination of $Ugcg^{loxP}$. The predicted outcome of Cre recombination is shown at the bottom. **B**: Identification of Cre-mediated recombination of the $Ugcg^{loxP}$ allele in brain (left panel). Genomic DNA from cerebellum and cerebrum of 8-week-old L7UgcgKO mice were subjected to PCR analysis using primers 1 and 3. Identification of the $Ugcg^{loxP}$ allele (right panel). Tail DNA from $Ugcg^{loxP/+}$: $L7\text{-}Cre^{tg/0}$ and $Ugcg^{loxP/loxP}$: $L7\text{-}Cre^{tg/0}$ mice were subjected to PCR analysis using primers 1 and 2. **C**: An L7-Cre mouse was bred with a Rosa26-lacZ reporter mouse, and Cre expression in the cerebellum of the resulting progeny was assessed for β-galactosidase activity. In the sagittal sections from mice 1–3 postnatal weeks old, blue-colored staining indicates Purkinje cell-specific Cre expression. Scale bars: 2 mm (lower panels); 1 mm (upper panels).

using a peristaltic pump. The perfused brain tissues were post-fixed in 4% PFA in 0.1 M phosphate buffer overnight at 4°C and embedded in 5% low-melting agarose gel. Sagittal sections of the cerebellum were cut at 50 μm using a LEICA microtome and stored in phosphate-buffered saline (PBS) at 4°C. In a few cases cerebellar coronal sections were cut. Free-floating sections of cerebellum were blocked for non-specific binding with PBS containing 0.1% (v/v) Triton X-100 and 10% (v/v) goat serum and incubated with primary antibody at 4°C overnight. The sections were washed and incubated with a species-appropriate secondary antibody (AlexaFluor-conjugated anti-rabbit, antirat, or anti-mouse IgG) at room temperature for 120 min, washed extensively, mounted onto glass slides with Immu-mount (Shandon, Inc., Pittsburgh, PA), and examined with fluorescent light microscopes. For some sections, cell nuclei were counterstained with 4′,6′-diamidino-2-phenylindole (DAPI; Nacalai Tesque Inc., Kyoto, Japan). For sodium channel and Caspr staining, PFA-perfused brains were cryoprotected with 30% sucrose in PBS (pH 7.4) for 24 h at 4°C, as described previously (Hoshi et al., 2007). After embedding in optimal cutting temperature (OCT)-mounting medium, the blocks were cut in 8-μm-thick sections.

For hematoxylin and eosin (HE) staining, PFA-perfused brains were kept in the same PFA fixative solution for one week, and then embedded in paraffin. Paraffin-embedded brains were sectioned at a thickness of 5 μm and processed for H&E staining. For X-gal staining, the brains were perfused with ice-cold PBS and 30% sucrose, dissected, and rapidly frozen in mounting medium. Cryostat sections (15–20 μm) were prepared and postfixed for 5 min in 4% PFA in PBS. The fixed sections were washed and subjected to X-Gal staining overnight at room temperature. The X-Gal staining solution comprised 1 mg/mL X-Gal (4-chloro-5-bromo-3-indolyl-b-galactosidase), 4 mM $K_4Fe(CN)_6{\cdot}3H_2O$, 4 mM $K_3Fe(CN)_6$, and 2 mM $MgCl_2$ in PBS. The slides were washed with PBS twice and once in distilled water, and then counterstained with eosin.

Electron Microscopy

Animals were perfused intracardially through the left ventricle with a fixative containing 2.5% (v/v) glutaraldehyde and 2.0% (w/v) PFA in 0.1 M phosphate buffer (pH 7.4). Cerebellums were dissected and postfixed by immersion in the same fixative overnight at 4°C then sagittal 50-μm sections of the cerebellar vermis were prepared. After osmification in a 1% (w/v) osmium tetroxide solution, the specimens were dehydrated through a graded alcohol series and embedded in Epon 812 (TAAB Laboratories, Aldermaston, Berks, UK). Semithin sections were collected and stained with 0.5% (w/v) toluidine blue in 0.1 M phosphate buffer (pH 7.4). Ultrathin sections were cut using an Ultracut microtome (Leica EM-UC6) and stained with uranyl acetate and lead citrate for contrast. The sections were examined with a transmission electron microscope (Hitachi H-7100 and H-7650).

Western Blot

Cerebellar extracts were prepared in 50 mM Tris-HCl (pH 7.4), 5 mM EDTA, and one tablet of Complete mini/25 mL (protease inhibitors; Roche Diagnostics). Samples were mixed with Laemmli buffer with or without (for anti-myelin-associated glycoprotein [MAG]) 2-mercaptoethanol. SDS–PAGE was performed, and separated proteins were transferred onto polyvinylidene difluoride membranes and subjected to immunoblotting with individual primary antibodies, including anti-MAG, anti-myelin basic protein (MBP), and antialpha tubulin (internal control). Immunoreactivity was visualized with HRP-conjugated secondary antibodies and a chemiluminescence detection system, according to the manufacturer's instructions (Millipore).

Antibodies

The following primary antibodies were used: mouse monoclonal anti-cytochrome c (clone 6H2.B4); mouse anti-GM130 (BD Transduction Laboratories, San Diego, CA); mouse anti-α-tubulin; mouse antipan sodium channel; mouse antisynaptophysin (Sigma, St. Louis, MO); mouse anticalbindin D28k (Swant, Bellinzona, Switzerland); mouse anti-TuJ1 (Covance, Princeton, NJ); mouse antikinesine heavy chain; mouse anti-MAG; rabbit polyclonal anti-calbindin D28k; rabbit anti-glutamate receptor delta 1/2 (GluRδ1/2); rat anti-MBP (Chemicon International, Temecula, CA); rabbit anti-Caspr (Abcam, Cambridge, MA); and rabbit anti-GFAP (Dako). Rat anti-inositol 1, 4, 5-triphosphate receptor 1 (IP3R1, clone 18A10) antibody was kindly provided by Dr. K. Mikoshiba. Rabbit polyclonal antibody to the C terminus (amino acids 372-394) of human GlcCer synthase (GlcT-1) was generated according to Marks et al. (1999).

Statistics

Data were expressed as means ± S.E.M. Significant differences between mean values were evaluated using two-tailed, unpaired Student's *t* tests.

RESULTS

Purkinje Cell-Specific Glycosphingolipid Deletion in L7UgcgKO Mice

To ensure that Cre was exclusively expressed in Purkinje neurons, we crossed L7-Cre mice with Rosa26-lacZ reporter mice and monitored Cre expression in their double-transgenic progeny (Fig. 1C). X-Gal staining for β-galactosidase activity indicated that Cre was exclusively expressed in Purkinje neurons of adult mice. Cre expression began two weeks after birth (postmitotic stage), becoming stronger and reaching a plateau four weeks after birth. The expression was highly specific for Purkinje neurons, all of which were positive for X-gal

staining in the brains of four-week-old double transgenic mice. A similar pattern of X-gal staining was observed in cerebellar coronal sections. We detected no X-gal staining in any other neurons in the brain. However, weak signals were detectable in retina, as reported by Oberdick et al. (1990).

Ugcg$^{loxP/loxP}$: *L7-Cre*$^{tg/0}$ mice (L7UgcgKO) comprised about 50% of the litter, indicating no prenatal death (see Methods). PCR analysis detected Cre recombination in cerebellum, but not cerebrum, in 8-week-old KO mice (Fig. 1B). Immunostaining against GlcT-1 (a Golgi-localized protein) verified that the Golgi apparatus of the Purkinje cells of L7UgcgKO mice lacked GlcT-1 immunoreactivity (Fig. 2D–F, P–R). Other cells in the molecular and granule layers, however, were GlcT-1 immunoreactive (arrowheads, Fig. 2D–F, J–L). Furthermore, in contrast to control mice (*Ugcg*$^{loxP/}$: *L7-Cre*$^{tg/0}$), in L7UgcgKO mice Purkinje cells lacked P-path antibody immunostaining (Fig. 2V–X). P-path antibody is an antibody that recognizes O-acetyl-GD3, an anabolite of glucosylceramide that is enriched in Purkinje cells (Leclerc et al., 1992). Thus, the immunohistochemical analysis confirmed the Purkinje cell-specific deletion of GlcCer synthase and absence of corresponding lipids.

Purkinje Cells With an L7-Promoted Ugcg Deletion Showed Numerous Axonal Swellings

Although the cerebellum of 22-week-old L7UgcgKO mice remained morphologically intact (Fig. 3C), Purkinje cell loss was evident (Fig. 3D,H,I), with increased GFAP expression (Supp. Info. Fig. 2). However, significant Purkinje cell loss was not observed in 14-week-old mutant mice (Fig. 3F,I), indicating that the loss of Purkinje cells occurred sometime between 14 and 22 weeks after birth. Despite Purkinje cell degeneration, 23- to 39-week-old mutant mice showed no motor deficits in an open-field test and rotor-rod test (Supp. Info. Fig. S1).

In comparison with the Purkinje cell axons of normal, age-matched mice, those of 14-week-old L7UgcgKO mice possessed numerous swellings (Fig. 4; mean ± SD swellings/section in lobule V: 14-week-old control mice, 1.0 ± 1.0; 14-week-old KO mice, 16.6 ± 5.9; 22-week-old control mice, 2.9 ± 2.3; and 22-week-old L7UgcgKO mice, 31.2 ± 10.6 swellings/section. Nine sections from three mice in each group). These swollen axons were located proximal to somata in the granular layer and were located distally in the deep cerebellar nuclei. These findings indicated that the deletion of GSLs led to axonal defects prior to Purkinje cell loss.

In contrast to the significant axonal degeneration, we did not observe dendritic degeneration in our light microscopy analysis of anticalbindin D28k immunofluorescent-stained sections (see Fig. 5). To further evaluate changes in dendrites, we examined the expression patterns of the glutamate receptor GluRδ1/2 and synaptophysin. There were no differences in localization or immunostaining intensity of either GluRδ1/2 or synaptophysin between 14-week-old control and L7UgcgKO mice (Fig. 5B,C,E,F). Thus, the *Ugcg* deletion had little effect on Purkinje cell dendrites. Apparently the *Ugcg* deletion elicits differential effects on dendritic and axonal compartments, with axons being particularly vulnerable to GSL deficiency.

Mitochondria, Synaptophysin, and Kinesin Heavy Chain Accumulate in Swollen Axons

Disruption of axonal transport causes axonal enlargement and aberrant accumulation of cargo proteins, mitochondria, and synaptic vesicles that travel to or from the axon terminal (Yagashita, 1979). To determine whether mitochondria accumulate in the swollen axons of L7UgcgKO mice, we immunostained cerebellar sections with an antibody against cytochrome c, a marker for mitochondria. The axonal swellings in L7UgcgKO mice showed enhanced cytochrome immunoreactivity compared with those in control mice (Fig. 6F), indicating that mitochondria did indeed accumulate within the axonal swellings. Furthermore, immunostaining of the synaptic vesicle protein synaptophysin and the microtubule-associated motor protein kinesin heavy chain revealed that both of these proteins also accumulated within axon swellings (Fig. 6D,E). The accumulation of these cargo molecules and organelles indicated that the mutant mice had axonal transport defects.

To further assess the effect of the GlcT-1 deletion, we examined the ultrastructure of the axonal swellings of L7UgcgKO mice. Electron microscopy revealed that the axonal swellings contained accumulated aberrant membrane structures and abnormal organelles (Fig. 6G,H). Taken together, the immunofluorescence and electron microscopy analyses show that disruption of GSLs synthesis led to axonal transport defects.

Some Axons in the Mutant Mice Were Surrounded by Two Concentric Myelin Sheaths

In L7UgcgKO mice, severe demyelination was not observed, even of swollen axons. Immunoblot analysis of cerebellar extracts revealed that myelin proteins (MBP and MAG) were present in similar amounts in control and KO mice (data not shown). In L7UgcgKO mice, however, paranodal junctions were disrupted and paranodal loops were detached from the axonal plasma membrane (Fig. 7B–D), indicating reduced adhesion between glial loops and axons.

Next, we examined Caspr localization specifically on Purkinje cell axons by co-immunostaining with IP3R1, a Purkinje cell marker (Maeda et al., 1988). Caspr was a useful marker for assessing the integrity of paranodal junctions on myelinated axons. Lengths of Caspr clusters in 17- to 22-week-old L7Ugcg KO mice were significantly shorter than those of control mice (Fig. 7E). These results are consistent with the loss of transverse bands in the paranodal loops (see Fig. 7). Furthermore, sodium channel clusters were elongated in the 17- to

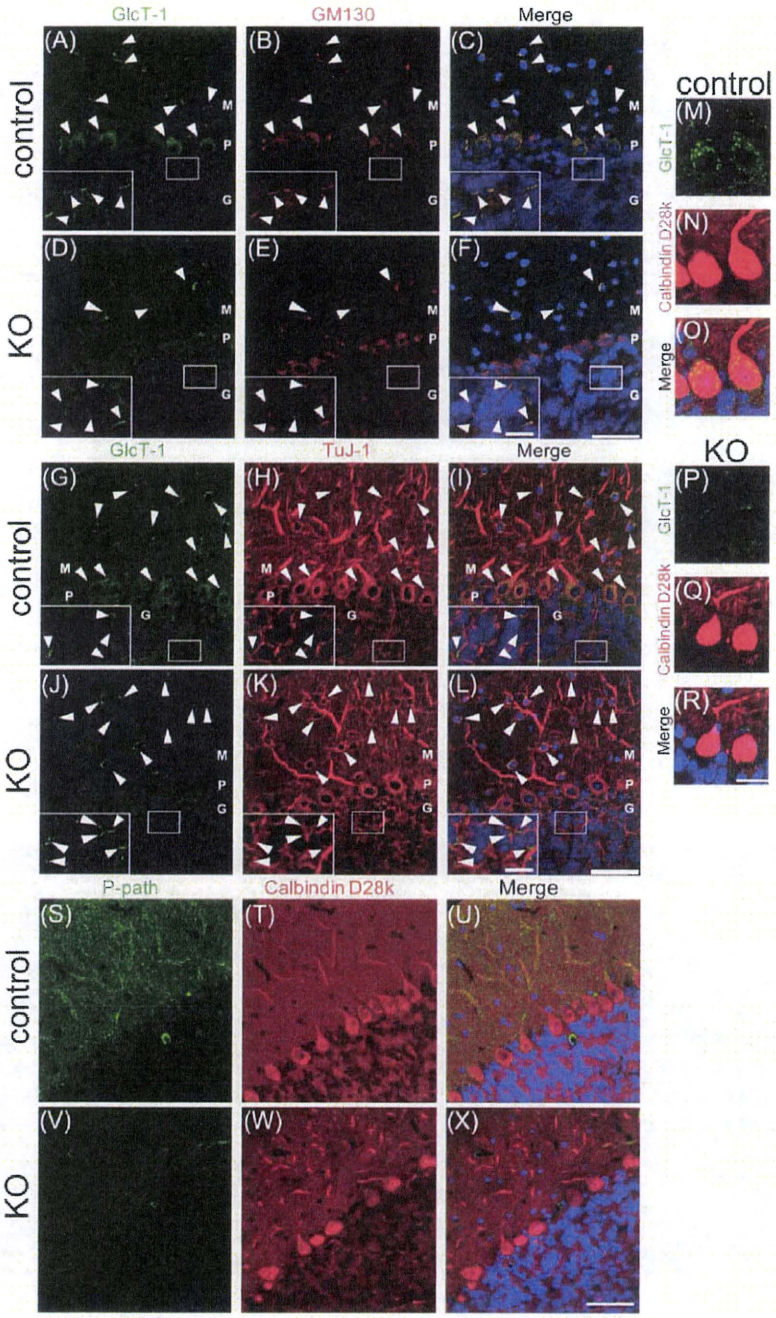

Fig. 2. Deletion of glucosylceramide synthase (GlcT-1) and an anabolite of glucosylceramide, o-acetyl GD3 (P-path antigen), were confirmed in eight-week-old Purkinje cell-specific *Ugcg* KO mice. **A–F**: Anti-GlcT-1 (A, D); anti-GM130 (Golgi apparatus marker, B,E); and merged (C,F). **G–L**: Anti-GlcT-1 (G, J); anti-TuJ-1 (neuronal marker, H, K); and merged (I, L). **M–R**: Anti-GlcT-1 (M, P); anti-calbindin D28k (N, Q); and merged (O, R). **S–X**: P-path (S, V); anti-calbindin D28k (T, W); and merged (U, X). Insets show high-magnification images of the white rectangular area in the granular layer. In the merged micrographs, cell nuclei were visualized with DAPI staining (blue). M, molecular layer; P, Purkinje cell layer; G, granule cell layer. Arrowheads point to GlcT-1-immunopostive cells. These results were observed in all mice of each genotype (n = 3). Scale bars: 50 μm (A-L, S-X); 20 μm (M-R); 10 μm (insets).

22-week-old KO mice, also suggesting disorganization of paranodal structures. These findings indicated that axonal GSLs contributed to Caspr localization and maintenance of nodal structures.

Notably, as shown in Fig. 8, excessive paranodal loops were formed on otherwise normal myelin sheaths. In longitudinally sectioned Purkinje cell axons, some myelin sheaths overlapped with neighboring sheaths and

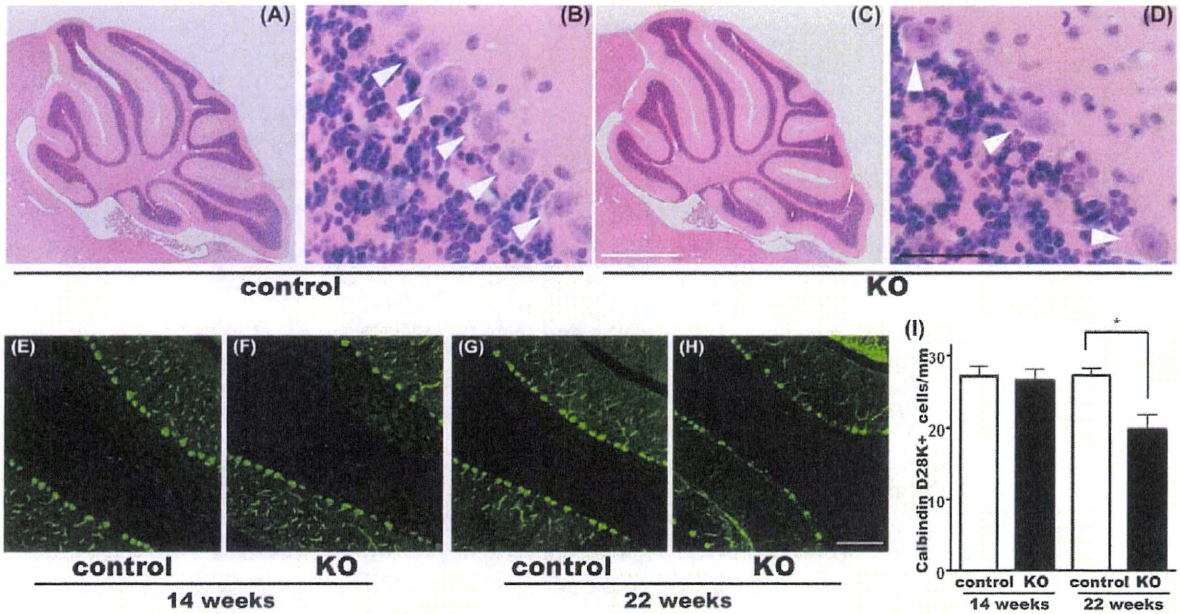

Fig. 3. Purkinje cell loss in L7UgcgKO mice. **A–D**: Hematoxylin and eosin (H&E)-stained cerebellar sections from 22-week-old control mice (A, B) and KO mice (C, D). Mid-sagittal sections through the entire extent of the cerebellum (A, C) show intact morphology in KO mice. Arrowheads point to Purkinje cell somata (B, D). Cerebellar sections from 14-week-old (**E, F**) and 22-week-old (**G, H**) control and KO mice were immunostained with anti-calbindin D28k, a Purkinje cell marker. L7UgcgKO mice showed Purkinje cell loss at 22 weeks (H), but no significant Purkinje cell loss at 14 weeks (F). Quantitation of Purkinje cells in lobule V of midsagittal sections of control and L7UgcgKO mice at 14 and 22 weeks; anticalbindin D28k stained Purkinje cells. The data are expressed as number of Purkinje cells per millimeter of Purkinje cell layer; $n = 3$, $^*P < 0.05$ (I). Scale bars: 1 mm (A, C); 50 μm (B, D); 100 μm (E–H).

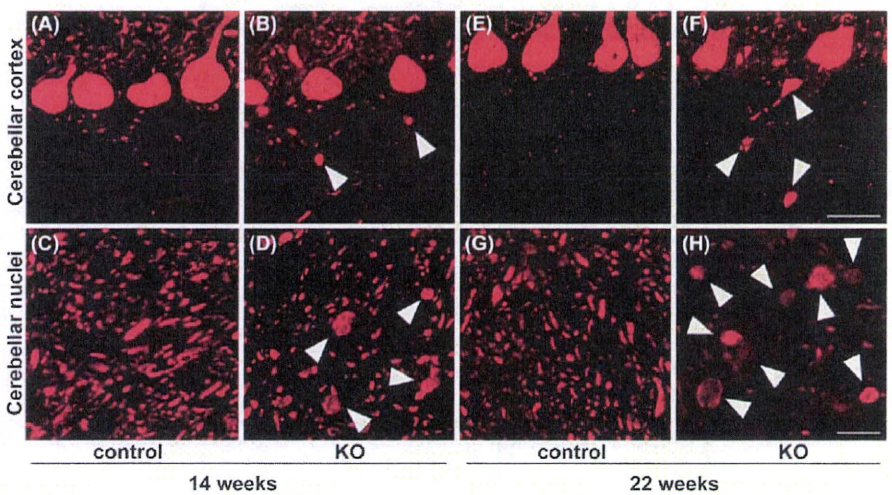

Fig. 4. Axonal swellings of Purkinje cells in L7UgcgKO mice. Cerebellar sections from 14-week-old and 22-week-old control and KO mice were immunostained with anti-calbindin D28k antibody. After postnatal week 14, axonal swellings were observed in both cerebellar deep nuclei (**D**, 14 weeks; **H**, 22 weeks) and cerebellar cortex (**B**, 14 weeks; **F**, 22 weeks). Control mice showed no axonal dystrophy in cerebellar cortex (**A**, 14 weeks; **E**, 22 weeks) or deep cerebellar nuclei (**C**, 14 weeks; **G**, 22 weeks). Arrowheads indicate axonal swellings. Scale bars: 25 μm for cerebellar cortex; 10 μm for cerebellar nuclei.

with paranodal loop-like structures that were filled with cytoplasm (see Fig. 8). Transverse bands, which link paranodal myelin loops with axolemma, were absent in these paranodal loop-like structures (Fig. 8E). These structures were observed at both postnatal 14 and 22 weeks, suggesting that the excessive paranodal loops and doubly-myelinated regions were formed prior to Purkinje cell loss.

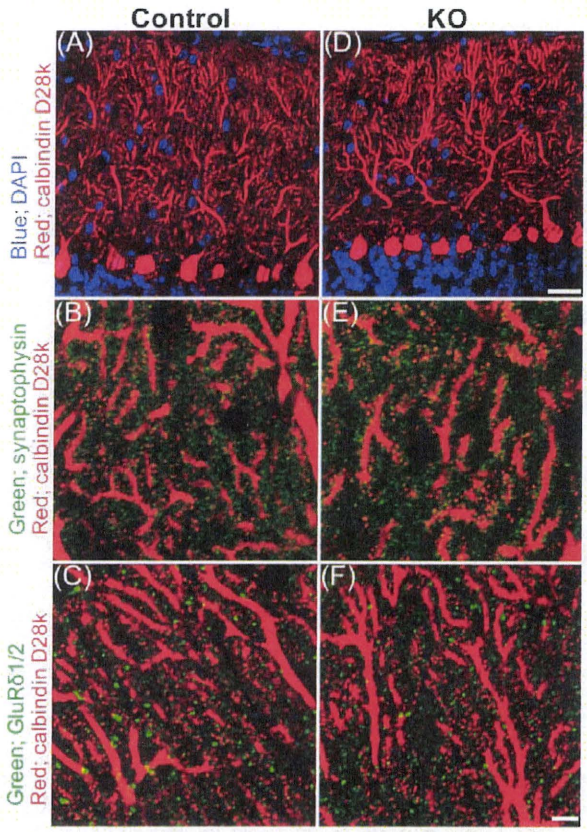

Fig. 5. *Ugcg* deletion had little effect on dendritic tree morphology. Immunofluorescent staining of cerebellar sagittal sections from 14-week-old L7UgcgKO mice showed normal localization and appearance of GluRδ and synaptophysin. The dendrites (red, ant-icalbindin D 28k immunostaining) of both wild-type and L7UgcgKO mice displayed comparable anti-synaptophysin (**B, E**; green) and anti-GluRδ1/2 (**C, F**; green) immunostaining. Nuclei were labeled with DAPI (**A, D**; blue). These results were observed in all mice of each genotype ($n = 3$). Scale bars: 50 μm for low magnification panels (A, D); 10 μm for high magnification panels (B, C, E, F).

DISCUSSION

GSLs, in particular the GlcCer-based GSLs, occur as sialic acid-containing gangliosides in the brain at a much higher concentration than in other organs. They might, therefore, play an important role in the nervous system. The majority of membrane GSLs is derived from the precursor, GlcCer. Therefore *Ugcg*, the gene encoding the glucosylceramide synthase (GlcT-1) that catalyzes the initial step of GSL biosynthesis, is a key regulator of total GSL synthesis. To elucidate the physiological roles of GSLs in neurons, we generated GlcT-1 conditional knockout mice using the Cre-loxP system. Given that GlcT-1 is essential for embryo survival, we decided to generate a Purkinje neuron-specific mutation of the *Ugcg* gene using L7-Cre transgenic mice.

In Purkinje cell-specific *Ugcg* KO mice, Purkinje cells started to degenerate 14–22 weeks after birth. This observation suggested that *Ugcg* is required for the maintenance of Purkinje cells. However, Purkinje cells survived for up to several weeks after *Ugcg* gene deletion, raising the possibility that GlcT-1 loss is not the immediate cause of the neuronal degeneration.

Before the Purkinje cell loss, we observed axonal swellings in Purkinje cells. Although axonal degeneration is considered to be diagnostic of neuronal cell death, recent studies have suggested that axonal defects are primary events that occur prior to overt neuronal degeneration following CNS injury, toxicity, genetic defects, and neurodegenerative disorders, including Alzheimer's disease (Coleman, 2005; Stokin et al., 2005). However, GlcT-1 is decreased in the brains of Alzheimer's disease patients (Marks et al., 2007), and mutant presenilin 1, which is associated with familial Alzheimer's disease, can cause the degradation of GlcT-1 protein (Mutoh et al., 2006). It is, therefore, likely that mutant presenilin 1 causes axonal defects by degrading GlcT-1 protein. Consistent with this premise is the finding that Alzheimer presenilin 1 mutations impair kinesin-based axonal transport (Lazarov et al., 2007; Pigino et al., 2003), which in turn leads to axonal swellings.

At 2.5 months of age, *St3gal5/B4galnt1* double KO mice display axonal spheroids in Purkinje cells and vacuoles in white matter (Yamashita et al., 2005b). The brains of these mice also accumulate lactosylceramide and sulfated lactosylceramide, SM3 (Yamashita et al., 2005b). Although our L7UgcgKO mice lacked all GlcCer-based GSLs, axonal swellings were not detected in 8-week-old mice (data not shown). Moreover, no vacuoles were observed in the mutant mice, even 22 weeks after birth. The relatively mild phenotype of L7UgcgKO mice compared with germline *St3gal5/B4galnt1* double-KO mice suggests that the GlcCer-based GSLs of non-neuronal cells may be essential for the maintenance of neuronal cells. Alternatively, deletion of GSLs during development may affect mature neurons at later stages. Consistent with this idea is the observation that mice in which *Ugcg* was conditionally deleted using Nestin-Cre (which is expressed during embryogenesis in the neural precursors of both neurons and glia) display more severe phenotypes (Jennemann et al., 2005), leading to neuronal degeneration and death of the mice by postnatal Day 21. These reports, together with our own findings, support the view that GSL expression during embryonic stages and/or in non-neuronal cells is required for the proper development and function of mature neurons.

In our L7UgcgKO mice, axonal swellings occurred prior to Purkinje cell loss, indicating that the axonal swellings were not secondary to neuronal degeneration. It is important to note that axonal transport defects contribute to axonal dystrophy (Coleman 2005; Stokin et al., 2005). In L7UgcgKO mice, microtubule transport cargo and machinery-such as cytochrome c, synaptophysin, and kinesin heavy chain-accumulated at axonal swellings, which is indicative of aberrant axonal transport. These observations suggest that suppression of GlcT-1 leads to axonal transport defects. Recent work indicates that cholesterol-rich microdomains are essential for synaptic vesicle sorting and that synaptic vesicle proteins are localized to cholesterol-rich microdomains (Chamber-

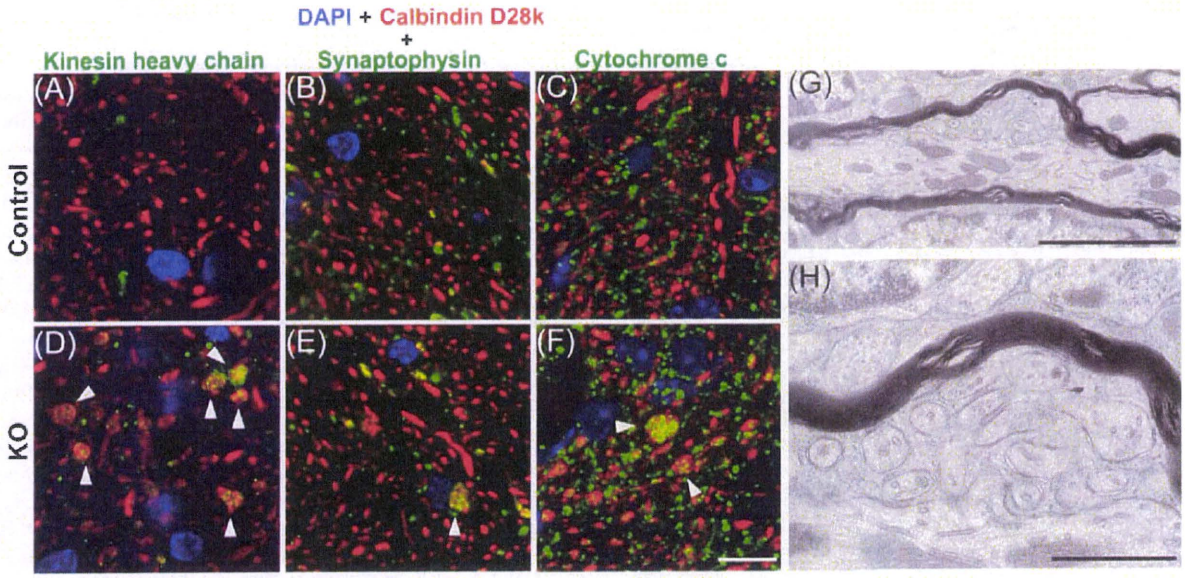

Fig. 6. Intense staining for mitochondria, synaptic vesicles, and kinesin heavy chain were observed in axonal swellings, suggesting that axonal transport was severely defective in L7UgcgKO mice. Cerebellar sections were co-immunostained with anticalbindin D28k (red) and antibodies against cargo markers (green), such as anti-kinesin heavy chain (**A, D**); antisynaptophysin (**B, E**); or anticytochrome c (**C, F**). Nuclei were labeled with DAPI (blue). Arrowheads indicate axonal swellings. Scale bar: 10 μm (A–F). Transmission electron micrograph showing the ultrastructure of a swollen axon from a L7UgcgKO mouse (**G, H**). Aberrant membrane structures and mitochondria accumulated within axonal swellings. These results were observed in all mice of each genotype ($n = 3$). Scale bars: 1 μm (G); 0.3 μm (H).

lain et al., 2001). Cholesterol/sphingolipid or GM1/cholera toxin B subunit complexes enhance microtubule-associated kinesin motor motility (Klopfenstein et al., 2002). The axonal swellings observed in our KO mice may be due to microdomain disruption, since GSLs and cholesterol are major components of lipid microdomains.

On the other hand, axonal degeneration and myelin disorganization are closely related. Although we did not detect severe demyelination in L7UgcgKO mice, their paranodal junctions were malformed, having shorter Caspr clusters. Caspr mutant mice develop paranodal disruptions and axonal swellings accompanied by mitochondria accumulation and cytoskeletal disorganization (Garcia-Fresco et al., 2006). Thus, abnormal localization of Caspr in L7UgcgKO mice may result in axonal swellings.

Disruption of paranodal junctions was also observed in germline *B4galnt1* KO mice and *St3gal5/B4galnt1* double-null mice (Susuki et al., 2007; Yamashita et al., 2005b). Unlike these KO mice, which lack GSLs in both axons and myelin, our L7UgcgKO mice only lack axonal GSLs. Thus, axonal GSLs are definitely essential for maintaining axo-glial interactions at paranodal junctions and for proper attachment of paranodal loops on the axolemma with transverse bands in conjunction with other cell adhesion molecules. On the other hand, because some membrane proteins are localized in lipid rafts, deleting axonal GSLs might impair lipid raft-dependent interactions between axonal membranes and oligodendrocyte processes. Supporting this idea are the findings that GlcCer-based GSLs in axons and/or oligodendrocytes contribute to localization of Caspr, an axonal adhesion molecule, in lipid microdomain/lipid rafts at the paranodal junction (Susuki et al., 2007). Indeed, the disrupted axo-glial interactions exhibited by *Ugt8*- or *Gal3st1*-mutant mice further support the premise that GalCer-based GSLs, which are enriched in myelin, play important roles in the maintenance of paranodal structures and Caspr localization (Dupree et al., 1999; Hoshi et al., 2007). Additionally, *Ugt8*-KO mice also show significant reduction of raft-associated Caspr (Schafer et al., 2004). These findings, together with our own findings, support the view that GSLs in both axons and myelin may be required for proper localization of Caspr in lipid rafts. However, it is difficult to perform biochemical analysis of axonal adhesion molecules in lipid rafts, since Purkinje neurons are scarce in cerebellar cortex. Furthermore, the excessive partial myelination (with cytoplasmic loop-like structure) in the KO mice suggests that axonal GSLs may play an important role in providing signals required for proper myelination by oligodendrocytes.

Some axons in the mutant mice were surrounded by two concentric myelin sheaths. How do these unusual structures form? In principle there are two possibilities: (1) The additional myelin sheath might invade beneath a pre-existing sheath, between the inner loop and the axon surface at the node of Ranvier; or (2) the additional myelin sheath might envelop an entire axon-myelin unit without disrupting existing axon-oligodendrocyte interactions. We cannot definitively distinguish these two possibilities by examining static images. However, we strongly favor the latter mechanism, because at the time of the *Ugcg* gene deletion was induced (at three weeks of age), Purkinje cell axons are already ensheathed by compact myelin

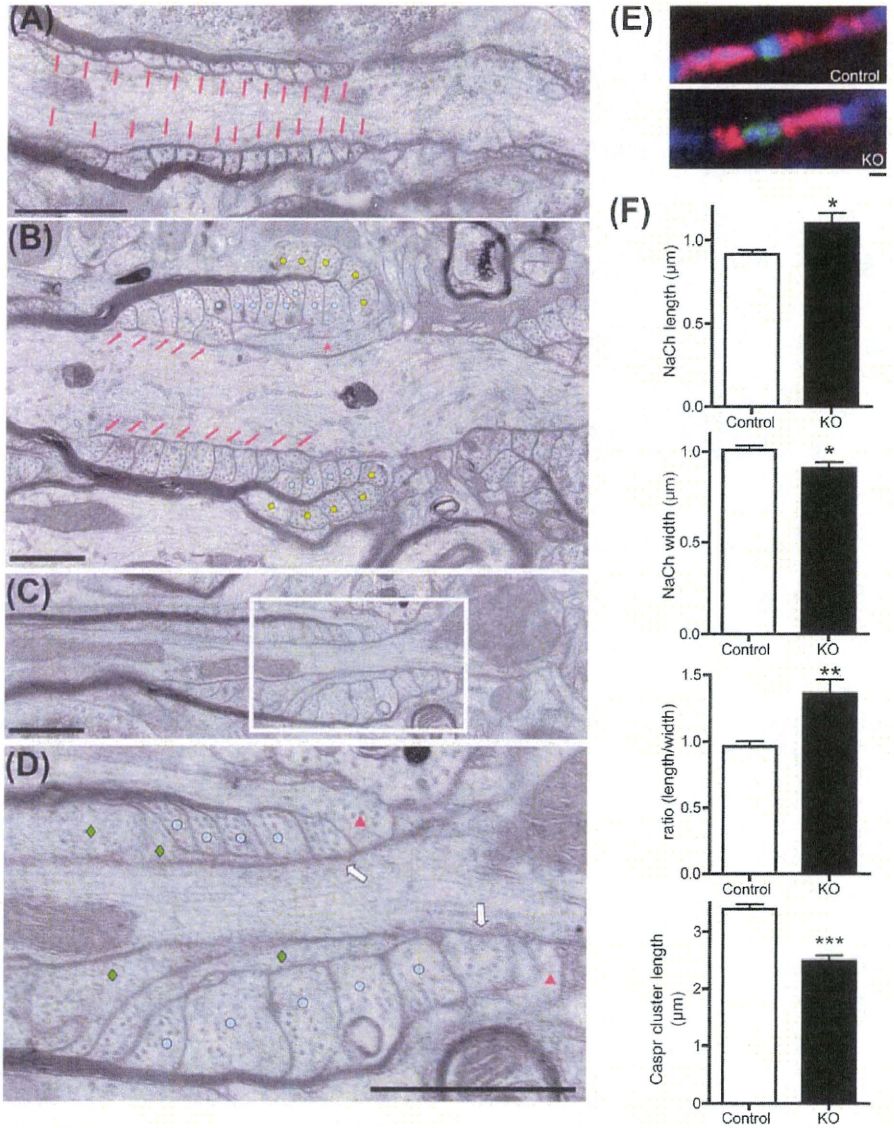

Fig. 7. L7UgcgKO mice exhibit ultrastructural abnormalities at paranodes. Longitudinal section through the paranodal portion of an axon from a control mouse (**A**) and KO mice (**B–D**). A: Normal ultrastructure of node and paranode of a control mouse. The cytoplasmic loops at the paranode are arranged orderly and are attached to the axolemma with a transverse band (TB, red arrow), indicating that at the paranode, the axon is enveloped by oligodendrocyte loops with a continuous TB. B: Abnormal paranode from a 22-week-old L7UgcgKO mouse. A compact myelin sheath consisting of 18 lamellae enwraps this axon. Of the 18 lamellae, nine of the lower and five of the upper paranodal cytoplasmic loops attach themselves onto the axolemma with TB (red arrows). The remaining loops, however, show abnormal contact with the axolemma (circles). The number of lower paranodal cytoplasmic loops contacting the axolemma with a TB is greater than that of the upper loops: nine vs. five normal loops, respectively. This indicates that TBs distribute discontinuously. Some loops (yellow circles) face away from the axon, presumably due to cytoplasmic loop abnormalities. A glial process (red triangle), presumably from an astrocyte, invades the space between the paranodal loops of the oligodendrocyte and axolemma. C: Abnormal paranode from a 14-week-old KO mouse. D: High-magnification image of the white rectangular area in (C). Two paranodal loops (white arrows) directly contact the axolemma. Other paranodal loops (blue circles), however, do not directly contact the axolemma. Deformed loops (green diamonds) attach to the axolemma without TBs. These structures indicate abnormal arrangement of paranodal cytoplasmic loops. These results were observed in all mice of each genotype ($n = 3$). Red triangles indicate processes that are presumably from an astrocyte. **E**: Cerebellar sections were co-immunostained with anti-IP3R1 (blue), anti-Caspr (red), and anti-pan sodium channel (green) antibodies. Elongated sodium channel clusters and shorter Caspr clusters were observed in L7UgcgKO mice. **F**: Quantitation of sodium channel cluster length, width, length-to-width ratio, and Caspr cluster length in lobule V of mid-sagittal sections of 17- to 22-week-old control and L7UgcgKO mice ($n = 3$). $^{*}P < 0.05$; $^{**}P < 0.01$; $^{***}P < 0.001$ compared with control mice. Scale bar: 1 μm (A–E).

(Bouslama-Oueghlani et al., 2003). In addition, it seems inherently unlikely that the adhesion between an axon and myelin membrane, as well as the adhesion between adjacent myelin sheets, could easily be disrupted.

Our results strongly suggest that axonal GSLs are required for axon-myelin interactions at various developmental stages. The binding partner of axonal GSLs in oligodendrocytes is MAG (Yang et al., 1996). MAG is a

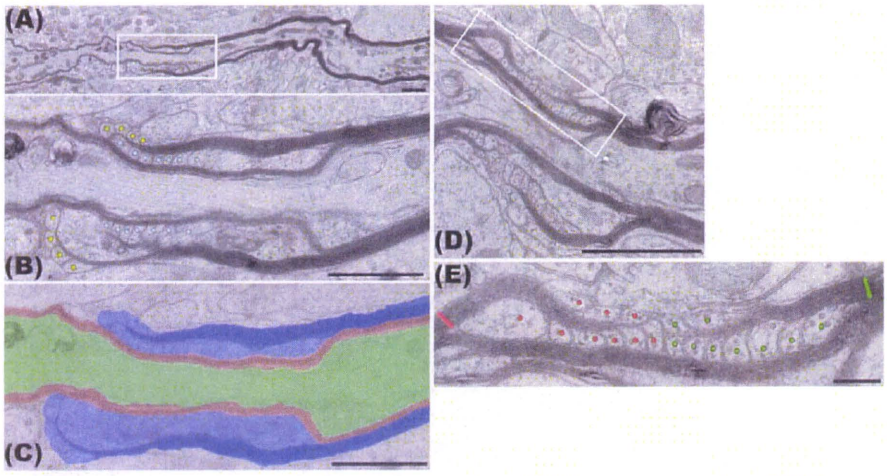

Fig. 8. Longitudinal section through axons from L7UgcgKO mice showing concentric, excessive myelin sheath formation with paranode-like structure. **A**: Doubly myelinated and hemiparanode-like structure from a 14-week-old KO mouse. **B**: High-magnification electron micrograph of the white rectangular area in Panel A. Myelin lamellae of outer myelin sheaths (dark blue, Panel **C**) terminate with cytoplasm filled paranode-like loops (circles in this panel; light blue, Panel C) on inner myelin sheaths (red, Panel C). D: Excessive paranode-like loops from a 22-week-old KO mouse. **E**: High-magnification electron micrograph of the white rectangular area in Panel D. On the left-hand side bilateral paranodal loop-like structures filled with cytoplasm marked with red circles are derived from nine-layered myelin lamellae (red bar); those marked with green circles are from nine-layered myelin lamellae coming from the right-hand side (green bar). These paranodal-like loops attach onto the inner compact myelin sheaths, i.e., the original myelin sheath. This symmetrical arrangement of loops is similar to that at the node of Ranvier. These results were observed in all mice of each genotype ($n = 3$). Scale bars: 1 μm (A–C); 0.5 μm (D,E).

type 1 transmembrane glycoprotein localized in periaxonal oligodendrocyte membranes in contact with axons. MAG-null mice make multiple myelin sheaths (Bartsch et al., 1995) similar to those observed in L7UgcgKO mice, suggesting that GSL binding to MAG regulates the myelin configuration and maintenance of axo-glial interactions. Schnaar and his associates reported that, among many ganglioside species tested, the α-series gangliosides GQ1b alpha and GD1 alpha were much more potent than GT1b or GD1a in supporting MAG-mediated cell adhesion (Ito et al., 2003). Since GD1 alpha is enriched in Purkinje cells (Furuya et al., 1994), the loss of adhesion mediated by interactions between MAG and GD1 alpha may underlie abnormal myelin morphology. Furthermore, cross sections of *Ugt8*-KO mice show that these mice have multiple myelinated axons (Bosio et al., 1998). Examining the spiraling direction in cross sections is necessary in order to determine whether multiple myelin sheaths originate from the same sheath or from two different myelin sheaths. A morphology characterized by spiraling in the same direction may result from the sheath carrying incisures parallel to the inner and outer loops of the sheaths (Hirano and Dembitzer, 1967). By contrast, a morphology characterized by spiraling in the opposite direction may represent two different concentric sheaths. Bosio et al. (1998) proposed that in mice with the *Ugt8* mutation multiple myelination of axons may be due to multiple myelin sheaths consisting of sheaths spiraling in both directions.

As described above, L7UgcgKO mice exhibited clear morphological defects in Purkinje cell axons. Their Purkinje cells, however, did not exhibit significant dendritic abnormalities. The localization of GluRδ1 or 2, a Purkinje cell-specific receptor at the synaptic cleft, and synaptophysin, a presynaptic marker, was indistinguishable in control and L7UgcgKO mice. These results suggest that the *Ugcg* null mutation in Purkinje cells results in axonal dystrophy at early stages of degeneration. However, GSLs have been suggested to play roles in dendritic functions such as improved learning, long-term potentiation (LTP), and synaptic transmission (Fujii et al., 2002). Internalization of AMPA receptors in dendrites are regulated by lipid microdomains (Hering et al., 2003). Interestingly, the cultured embryonic hippocampal neurons of Nestin-Cre *Ugcg* conditional-null mice have short dendrites (Jennemann et al., 2005). Therefore, future studies of L7UgcgKO mice should include an examination of synaptic transmission and neuronal plasticity such as long-term depression.

In this study, deleting GSLs specifically in neurons but not in oligodendrocytes caused axonal swellings, paranodal disruption, and double myelination. Our findings suggest that *de novo* synthesis of GSLs in neurons, but not in non-neuronal cells, is essential for the maintenance of axonal homeostasis and normal myelin formation, thereby providing fresh insight into the pathophysiological basis of neural diseases that are characterized by axonal degeneration and impaired myelination.

ACKNOWLEDGMENTS

The authors thank Prof. William D. Richardson (Wolfson Institute for Biomedical Research and Research Department of Cell and Developmental Biology, University College London) for helpful comments on the manuscript; Dr. S. Nakazawa (NIH) for generating L7Cre

transgenic mouse lines; Ms. Masako Suzuki (Aging Regulation Team, Tokyo Metropolitan Institute of Gerontology) for technical help on the examination of L7-Cre expression; Dr. Katsuhiko Mikoshiba (Labolatory for Developmental Neurobiology, RIKEN, BSI) for the generous gift of IP3R1 antibody; and Mr. Shuichiro Hayashi (The Center for EM and Bio-Imaging Research, Nano-Neuroanatomy, Iwate Medical University) for technical help on electron microscopy.

REFERENCES

Bartsch U, Montag D, Bartsch S, Schachner M. 1995. Multiply myelinated axons in the optic nerve of mice deficient for the myelin-associated glycoprotein. Glia 14:115–122.

Boldin S, Futerman AH. 1997. Glucosylceramide synthesis is required for basic fibroblast growth factor and laminin to stimulate axonal growth. J Neurochem 68:882–885.

Bosio A, Bussow H, Adam J, Stoffel W. 1998. Galactosphingolipids and axono-glial interaction in myelin of the central nervous system. Cell Tissue Res 292:199–210.

Bouslama-Oueghlani L, Wehrle R, Sotelo C, Dusart I. 2003. The developmental loss of the ability of Purkinje cells to regenerate their axons occurs in the absence of myelin: An in vitro model to prevent myelination. J Neurosci 23:8318–8329.

Chamberlain LH, Burgoyne RD, Gould GW. 2001. SNARE proteins are highly enriched in lipid rafts in PC12 cells: Implications for the spatial control of exocytosis. Proc Natl Acad Sci USA 98:5619–5624.

Coleman M. 2005. Axon degeneration mechanisms: Commonality amid diversity. Nat Rev Neurosci 6:889–898.

Dupree JL, Girault JA, Popko B. 1999. Axo-glial interactions regulate the localization of axonal paranodal proteins. J Cell Biol 147:1145–1152.

Freire E, Gomes FC, Jotha-Mattos T, Neto VM, Silva Filho FC, Coelho-Sampaio T. 2004. Sialic acid residues on astrocytes regulate neuritogenesis by controlling the assembly of laminin matrices. J Cell Sci 117(Part 18):4067–4076.

Fujii S, Igarashi K, Sasaki H, Furuse H, Ito K, Kaneko K, Kato H, Inokuchi J, Waki H, Ando S. 2002. Effects of the mono- and tetrasialogangliosides GM1 and GQ1b on ATP-induced long-term potentiation in hippocampal CA1 neurons. Glycobiology 12:339–344.

Furuya S, Irie F, Hashikawa T, Nakazawa K, Kozakai A, Hasegawa A, Sudo K, Hirabayashi Y. 1994. Ganglioside GD1 alpha in cerebellar Purkinje cells. Its specific absence in mouse mutants with Purkinje cell abnormality and altered immunoreactivity in response to conjunctive stimuli causing long-term desensitization. J Biol Chem 269:32418–32425.

Garcia-Fresco GP, Sousa AD, Pillai AM, Moy SS, Crawley JN, Tessarollo L, Dupree JL, Bhat MA. 2006. Disruption of axo-glial junctions causes cytoskeletal disorganization and degeneration of Purkinje neuron axons. Proc Natl Acad Sci USA 103:5137–5142.

Hering H, Lin CC, Sheng M. 2003. Lipid rafts in the maintenance of synapses, dendritic spines, and surface AMPA receptor stability. J Neurosci 23:3262–3271.

Hirano A, Dembitzer HM. 1967. A structural analysis of the myelin sheath in the central nervous system. J Cell Biol 34:555–567.

Hoshi T, Suzuki A, Hayashi S, Tohyama K, Hayashi A, Yamaguchi Y, Takeuchi K, Baba H. 2007. Nodal protrusions, increased Schmidt-Lanterman incisures, and paranodal disorganization are characteristic features of sulfatide-deficient peripheral nerves. Glia 55:584–594.

Ichikawa S, Hirabayashi Y. 1998. Glucosylceramide synthase and glycosphingolipid synthesis. Trends Cell Biol 8:198–202.

Inoue M, Fujii Y, Furukawa K, Okada M, Okumura K, Hayakawa T, Furukawa K, Sugiura Y. 2002. Refractory skin injury in complex knock-out mice expressing only the GM3 ganglioside. J Biol Chem 277:29881–29888.

Ito H, Ishida H, Collins BE, Fromholt SE, Schnaar RL, Kiso M. 2003. Systematic synthesis and MAG-binding activity of novel sulfated GM1b analogues as mimics of Chol-1 (alpha-series) gangliosides: Highly active ligands for neural siglecs. Carbohydr Res 338:1621–1639.

Jennemann R, Sandhoff R, Wang S, Kiss E, Gretz N, Zuliani C, Martin-Villalba A, Jager R, Schorle H, Kenzelmann M, Bonrouhi M, Wiegandt H, Gröne HJ. 2005. Cell-specific deletion of glucosylceramide synthase in brain leads to severe neural defects after birth. Proc Natl Acad Sci USA 102:12459–12464.

Klopfenstein DR, Tomishige M, Stuurman N, Vale RD. 2002. Role of phosphatidylinositol(4,5)bisphosphate organization in membrane transport by the Unc104 kinesin motor. Cell 109:347–358.

Lazarov O, Morfini GA, Pigino G, Gadadhar A, Chen X, Robinson J, Ho H, Brady ST, Sisodia SS. 2007. Impairments in fast axonal transport and motor neuron deficits in transgenic mice expressing familial Alzheimer's disease-linked mutant presenilin 1. J Neurosci 27:7011–7020.

Leclerc N, Schwarting GA, Herrup K, Hawkes R, Yamamoto M. 1992. Compartmentation in mammalian cerebellum: Zebrin II, P-path antibodies define three classes of sagittally organized bands of Purkinje cells. Proc Natl Acad Sci USA 89:5006–5010.

Maeda N, Niinobe M, Nakahira K, Mikoshiba K. 1988. Purification and characterization of P400 protein, a glycoprotein characteristic of Purkinje cell, from mouse cerebellum. J Neurochem 51:1724–1730.

Marks DL, Wu K, Paul P, Kamisaka Y, Watanabe R, Pagano RE. 1999. Oligomerization and topology of the Golgi membrane protein glucosylceramide synthase. J Biol Chem 274:451–456.

Marks N, Berg MJ, Saito M, Saito M. 2008. Glucosylceramide synthase decrease in frontal cortex of Alzheimer brain correlates with abnormal increase in endogenous ceramides: Consequences to morphology and viability on enzyme suppression in cultured primary neurons. Brain Res.

Mutoh T, Hirabayashi Y, Mihara T, Ueda M, Koga H, Ueda A, Kokura T, Yamamoto H. 2006. Role of glycosphingolipids and therapeutic perspectives on Alzheimer's disease. CNS Neurol Disord Drug Targets 5:375–380.

Mutoh T, Tokuda A, Inokuchi J, Kuriyama M. 1998. Glucosylceramide synthase inhibitor inhibits the action of nerve growth factor in PC12 cells. J Biol Chem 273:26001–26007.

Oberdick J, Smeyne RJ, Mann JR, Zackson S, Morgan JI. 1990. A promoter that drives transgene expression in cerebellar Purkinje and retinal bipolar neurons. Science 248:223–226.

Pigino G, Morfini G, Pelsman A, Mattson MP, Brady ST, Busciglio J. 2003. Alzheimer's presenilin 1 mutations impair kinesin-based axonal transport. J Neurosci 23:4499–4508.

Schafer DP, Bansal R, Hedstrom KL, Pfeiffer SE, Rasband MN. 2004. Does paranode formation and maintenance require partitioning of neurofascin 155 into lipid rafts? J Neurosci 24:3176–3185.

Schwarz A, Futerman AH. 1997. Distinct roles for ceramide and glucosylceramide at different stages of neuronal growth. J Neurosci 17:2929–2938.

Sheikh KA, Sun J, Liu Y, Kawai H, Crawford TO, Proia RL, Griffin JW, Schnaar RL. 1999. Mice lacking complex gangliosides develop Wallerian degeneration and myelination defects. Proc Natl Acad Sci USA 96:7532–7537.

Stokin GB, Lillo C, Falzone TL, Brusch RG, Rockenstein E, Mount SL, Raman R, Davies P, Masliah E, Williams DS, Goldstein LS. 2005. Axonopathy and transport deficits early in the pathogenesis of Alzheimer's disease. Science 307:1282–1288.

Sugiura Y, Furukawa K, Tajima O, Mii S, Honda T, Furukawa K. 2005. Sensory nerve-dominant nerve degeneration and remodeling in the mutant mice lacking complex gangliosides. Neuroscience 135:1167–1178.

Susuki K, Baba H, Tohyama K, Kanai K, Kuwabara S, Hirata K, Furukawa K, Furukawa K, Rasband MN, Yuki N. 2007. Gangliosides contribute to stability of paranodal junctions and ion channel clusters in myelinated nerve fibers. Glia 55:746–757.

Vyas AA, Patel HV, Fromholt SE, Heffer-Lauc M, Vyas KA, Dang J, Schachner M, Schnaar RL. 2002. Gangliosides are functional nerve cell ligands for myelin-associated glycoprotein (MAG), an inhibitor of nerve regeneration. Proc Natl Acad Sci USA 99:8412–8417.

Yagashita S. 1979. Ultrastructural observations on axonal swelling in the human gracile nucleus. Virchows Arch A Pathol Anat Histol 382:217–226.

Yamashita T, Allende ML, Kalkofen DN, Werth N, Sandhoff K, Proia RL. 2005a. Conditional LoxP-flanked glucosylceramide synthase allele controlling glycosphingolipid synthesis. Genesis 43:175–180.

Yamashita T, Wada R, Sasaki T, Deng C, Bierfreund U, Sandhoff K, Proia RL. 1999. A vital role for glycosphingolipid synthesis during development and differentiation. Proc Natl Acad Sci USA 96:9142–9147.

Yamashita T, Wu YP, Sandhoff R, Werth N, Mizukami H, Ellis JM, Dupree JL, Geyer R, Sandhoff K, Proia RL. 2005b. Interruption of ganglioside synthesis produces central nervous system degeneration and altered axon-glial interactions. Proc Natl Acad Sci USA 102:2725–2730.

Yang LJ, Zeller CB, Shaper NL, Kiso M, Hasegawa A, Shapiro RE, Schnaar RL. 1996. Gangliosides are neuronal ligands for myelin-associated glycoprotein. Proc Natl Acad Sci USA 93:814–818.

OPEN ACCESS Freely available online

PLoS one

Impaired Auditory-Vestibular Functions and Behavioral Abnormalities of *Slitrk6*-Deficient Mice

Yoshifumi Matsumoto[1], Kei-ichi Katayama[1], Takehito Okamoto[2], Kazuyuki Yamada[3], Noriko Takashima[1], Soichi Nagao[2], Jun Aruga[1]*

1 Laboratory for Behavioral and Developmental Disorders, RIKEN Brain Science Institute (BSI), Wako-shi, Japan, **2** Laboratory for Motor Learning Control, RIKEN Brain Science Institute (BSI), Wako-shi, Japan, **3** Support Unit for Animal Experiments, RIKEN Brain Science Institute (BSI), Wako-shi, Japan

Abstract

A recent study revealed that Slitrk6, a transmembrane protein containing a leucine-rich repeat domain, has a critical role in the development of the inner ear neural circuit. However, it is still unknown how the absence of *Slitrk6* affects auditory and vestibular functions. In addition, the role of *Slitrk6* in regions of the central nervous system, including the dorsal thalamus, has not been addressed. To understand the physiological role of Slitrk6, *Slitrk6*-knockout (KO) mice were subjected to systematic behavioral analyses including auditory and vestibular function tests. Compared to wild-type mice, the auditory brainstem response (ABR) of *Slitrk6*-KO mice indicated a mid-frequency range (8–16 kHz) hearing loss and reduction of the first ABR wave. The auditory startle response was also reduced. A vestibulo-ocular reflex (VOR) test showed decreased vertical (head movement–induced) VOR gains and normal horizontal VOR. In an open field test, locomotor activity was reduced; the tendency to be in the center region was increased, but only in the first 5 min of the test, indicating altered adaptive responses to a novel environment. Altered adaptive responses were also found in a hole-board test in which head-dip behavior was increased and advanced. Aside from these abnormalities, no clear abnormalities were noted in the mood, anxiety, learning, spatial memory, or fear memory–related behavioral tests. These results indicate that the *Slitrk6*-KO mouse can serve as a model of hereditary sensorineural deafness. Furthermore, the altered responses of *Slitrk6*-KO mice to the novel environment suggest a role of *Slitrk6* in some cognitive functions.

Citation: Matsumoto Y, Katayama K-i, Okamoto T, Yamada K, Takashima N, et al. (2011) Impaired Auditory-Vestibular Functions and Behavioral Abnormalities of *Slitrk6*-Deficient Mice. PLoS ONE 6(1): e16497. doi:10.1371/journal.pone.0016497

Editor: Fabien Tell, The Research Center of Neurobiology-Neurophysiology of Marseille, France

Received October 14, 2010; **Accepted** December 20, 2010; **Published** January 26, 2011

Funding: This study was funded by RIKEN Brain Science Institute (BSI) and supported by the Japan Society for the Promotion of Science. The funders had no role in study design, data collection and analysis, decision to publish, or preparation of the manuscript.

Competing Interests: The authors have declared that no competing interests exist.

* E-mail: jaruga@brain.riken.jp

Introduction

Slitrk6 belongs to the Slitrk family of transmembrane proteins with neurite outgrowth modulating activities [1,2]. Structurally, Slitrk members share two leucine-rich repeat domains located amino-terminal to the transmembrane domain. In the carboxy-terminus, there are conserved tyrosine residues flanked by amino acid sequences similar to those in the carboxy-terminal domain of the Ntrk neurotrophin receptor [3]. Among the six *Slitrk* family genes (*Slitrk1–6*) in mice, *Slitrk6* shows a unique expression pattern, with strong expression in the inner ear and modest expression in the dorsal thalamus at both embryonic and postnatal stages [1,4–6].

A recent study revealed that Slitrk6 promotes innervation and survival of inner ear sensory neurons in part by modulating neurotrophin–Ntrk signaling [5]. *Slitrk6*-knockout (KO) mice showed reduced cochlear innervation. In the vestibule, the innervation to the posterior crista was often lost, reduced, or sometimes misguided. These defects were accompanied by the loss of neurons in the spiral and vestibular ganglia. This study addressed only the embryonic to early postnatal morphological phenotype of *Slitrk6*-KO mice, and analyses of any functional deficits caused by the developmental defects of the inner ear remain to be conducted.

Previous studies reported Slitrk family members as candidate genes controlling several neuropsychiatric disorders [7–13]. Considering the expression of *Slitrk6* in the mature central nervous system [1,2] (http://www.brain-map.org/), it is possible that *Slitrk6* has a role in the expression of higher brain functions.

In the present study, we evaluated the neurological characteristics of the *Slitrk6*-KO mouse by performing systematic behavioral analyses and physiological tests related to inner ear functions. The results revealed deficits in the auditory, vestibular, and cognitive functions of *Slitrk6*-KO mice. We discussed the biological significance of *Slitrk6* and the similarities of deficits in the KO mice to the phenotypes of some neurological diseases.

Results

General features of the *Slitrk6*-KO mouse

The *Slitrk6* null allele (*Slitrk6*$^{-}$) was generated by replacing its entire protein-coding region by a loxP sequence [5]. Both male and female *Slitrk6*-KO (*Slitrk6*$^{-/-}$) mice grew without showing any external abnormalities and were fertile [5]. A slight, but significant reduction in body weight was observed in the adult male mice (wild type [WT]: $n = 10$, 26.5±0.57 g [mean ± SE]; KO: $n = 10$, 24.6±0.19 g at 12 weeks old). However, the reason for this weight reduction is not clear. We used adult male *Slitrk6*-KO mice and

WT (*Slitrk6*$^{+/+}$) littermates for the behavioral and inner ear function tests. The behavioral tests are listed in Table 1.

Auditory function defects in *Slitrk6*-KO mice

Auditory brain-stem response (ABR) is an electrical signal reflecting the neuronal activities related to auditory information processing. The ABR method has been shown to be effective for assessing auditory function in mice [14]. We recorded ABRs in anesthetized mice with ear and scalp electrodes. The responses were recorded upon delivering sound stimuli with certain ranges of frequencies (2–24 kHz) and strength (10–80 dB). Figure 1A presents the ABR waves from WT and *Slitrk6*-KO mice. To determine the hearing function of *Slitrk6*-KO mice, we first measured the thresholds for the appearance of a recognizable wave representing ABR (Fig. 1B). The results indicated significant increments (ca. 20 dB) of the sound intensity threshold for 8-kHz (WT $=48.5\pm2.6$ [mean $\pm$ SE], KO $=62.2\pm2.22$; $P<0.01$, Mann-Whitney's *U*-test) and 16-kHz (WT $=17.1\pm1.84$, KO $=30\pm2.88$; $P<0.05$) stimuli, but not for 2-, 4-, and 24-kHz stimuli at 4 weeks of age. When the amplitude and latency values of peaks I, II, and III with an 80-dB stimulus were compared between WT and *Slitrk6*-KO mice (Fig. 1C top), there was a significant decrement in the peak I absolute values of 16-kHz (WT $=5.42\pm0.43$ [mean $\pm$ SE], KO $=3.55\pm0.31$; $P=0.0031$), 8-kHz (WT $=2.51\pm0.15$, KO $=1.36\pm0.16$; $P=0.00020$), and 4-kHz (WT $=2.58\pm0.09$, KO $=2.02\pm0.16$; $P=0.012$) stimuli-induced

Table 1. Summary of Slitrk6 KO behavioral analyses.

Test	Parameter	Comparison to WT mice
Home cage activity	whole day	n.s.
	light phase	increment in KO mice (08:00–09:00, $P<0.05$)
	dark phase	decrement in KO mice (23:00–01:00, $P=0.68$)
Open field	total distance	decrement in KO mice (first 5 min, $P<0.01$)
	moving speed	decrement in KO mice ($P<0.01$)
	time in center area (%)	increment in KO mice (first 5 min, $P<0.01$)
Hole-board test	active time	n.s.
	total distance (cm)	n.s.
	head-dip latency (s)	decrement in KO mice ($P<0.05$)
	number of head dips	n.s.
	head dipping duration (s)	increment in KO mice ($P<0.05$)
	rearing duration (s)	n.s.
	number of rearing episodes	n.s.
Elevated plus maze	total distance (cm)	n.s.
	entry number	n.s.
	time in open arm (%)	n.s.
	number of entry to open arm (%)	n.s.
Light–dark box	total distance (cm)	n.s.
	number of transitions	n.s.
	latency to transition to dark box	n.s.
	distance travelled in light box (%)	n.s.
	time spent in light box (%)	n.s.
Morris water maze	total distance (cm)	n.s.
	movement time (s)	n.s.
	latency to platform (s)	n.s.
Fear conditioning	context test	n.s.
	cued test	n.s.
Hot plate test	lick	n.s.
Tail flick test	flinch	n.s.
	jump	n.s.
Rota- rod test	rotation	n.s.
Startle response	startle response	decrement in KO mice (95–120 dB, $P<0.01$)
	initial/final	n.s.
	prepulse inhibition	n.s.
Social interaction	number of contacts	n.s.
Tail suspension	immobility time (%)	decrement in KO mice ($P<0.01$)
Forced swimming	immobility time (%)	n.s.

doi:10.1371/journal.pone.0016497.t001

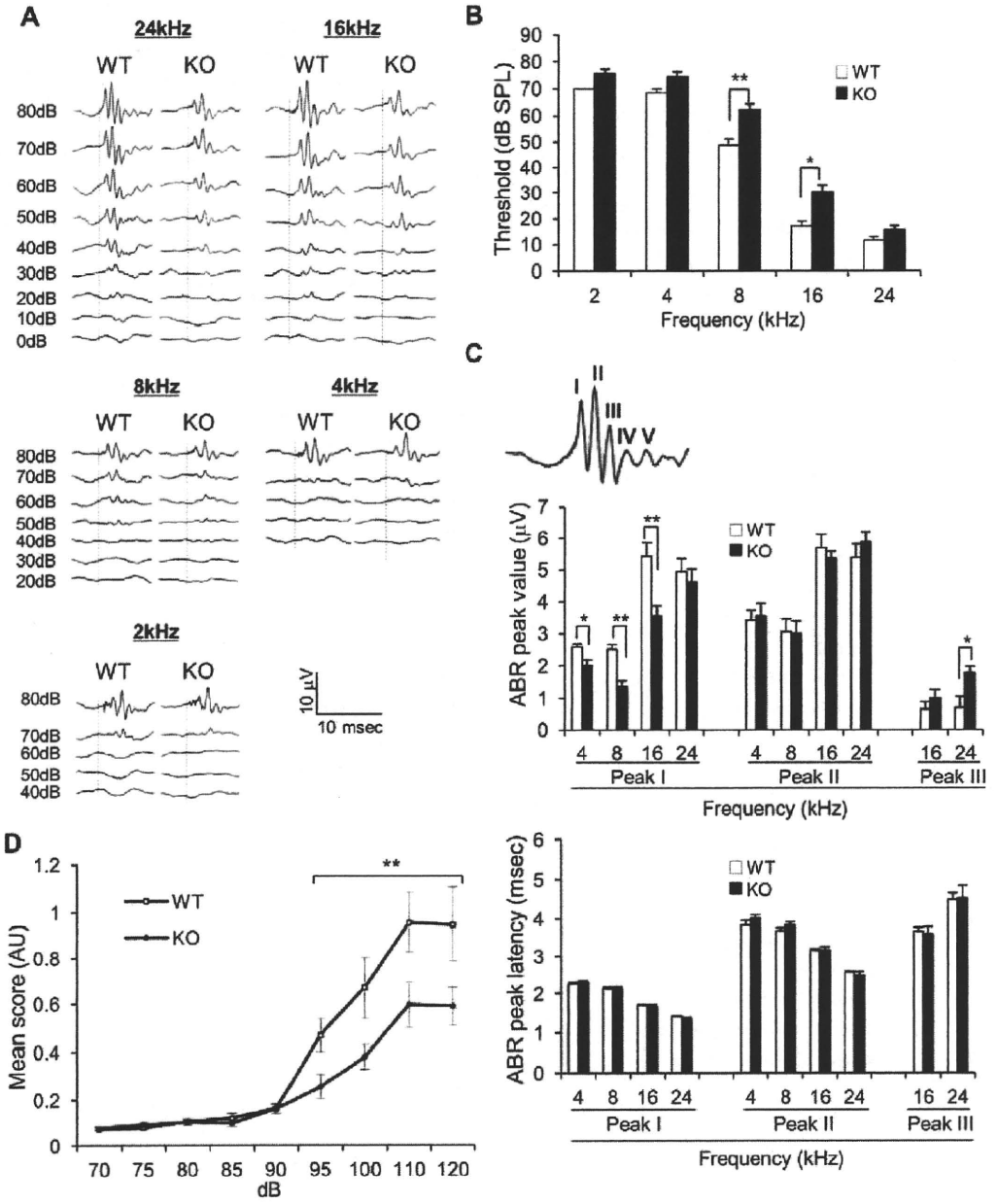

Figure 1. Auditory function abnormalities in *Slitrk6*-KO mice. (A) Representative waves of auditory brainstem response (ABR) from WT (left, $n=7$) and *Slitrk6*-KO (right, $n=9$) mice. ABR were recorded upon 0- to 80-dB sound pressure level (SPL) stimuli of 2, 4, 8, 16, and 24 kHz. The dash lines indicate the time of click presentation. The scale bars are shown at bottom right. (B) ABR thresholds in WT and *Slitrk6*-KO mice. *Slitrk6*-KO mice showed significantly higher thresholds to the 8- and 16-kHz stimuli than those of WT mice. (C) *Top:* Each peak number in a representative ABR wave. *Middle:* Comparison of the values of peaks I, II, and III between WT and *Slitrk6*-KO mice. Peak I of *Slitrk6*-KO mice was significantly reduced in the range of 8 to 16 kHz, and peak III was also significantly reduced at 24 kHz. *Bottom:* The latency to peaks I, II, and III. The latency did not show clear differences between WT and *Slitrk6*-KO mice. (D) Auditory startle response of WT ($n=10$) and *Slitrk6*-KO mice ($n=10$). *Slitrk6*-KO mice showed significantly lower startle responses to 95- to 120-dB sounds. $^{*}P<0.05$, $^{**}P<0.01$. All bars are mean ± standard error of the mean.
doi:10.1371/journal.pone.0016497.g001

responses in *Slitrk6*-KO mice (Fig. 1C middle). There also was a significant increment in the peak III absolute values for the 24-kHz stimulus (Fig. 1C middle; WT $=0.69\pm0.34$, KO $=1.76\pm0.20$; $P=0.015$). However, the peak latency was not significantly different between the two genotypes (Fig. 1C bottom).

Auditory startle response (ASR) was included in the auditory function analysis. We measured the ASR following white noise stimulation with various sound intensities (Fig. 1D; 70–120 dB on 65-dB background noise). Compared with WT mice, *Slitrk6*-KO mice showed significant decrements of ASR toward the stronger

sound stimuli (95–120 dB; $F_{1,18} = 9.7$, $P = 0.0059$, two-way ANOVA, main effect of genotype) but not toward the weaker ones (70–90 dB). While there was a clear difference in ASR between the genotypes, there were no significant differences in the prepulse (70, 75, and 80 dB) inhibition of ASR induced by a 120-dB stimulus (Table 1). Thus, both ABR and ASR results indicated that there was an auditory function deficit in the *Slitrk6*-KO mice.

Vertical vestibular function defects in *Slitrk6*-KO mice

A previous study revealed the frequent absence of vestibular nerve projection to the posterior crista in *Slitrk6*-KO mice [5]. Therefore, functions of the semicircular canal were investigated. We measured eye movements induced by rotation of the head on the plane of the horizontal semicircular canal, that is, the horizontal vestibulo-ocular reflex (hVOR), or on the plane perpendicular to the plane of the horizontal semicircular canal, the vertical vestibulo-ocular reflex (vVOR). The horizontal optokinetic response (hOKR), which shares the same neural circuit within the cerebellum as that of the hVOR, was measured as a reference. There were no clear differences in the hVOR or hOKR gains and phases between WT and *Slitrk6*-KO mice (Fig. 2A, B). For the vVOR, however, *Slitrk6*-KO mice showed significantly decreased gains at all four frequencies examined (Fig. 2C; $F_{1,12} = 11.7$, $P = 0.0051$, two-way ANOVA, main effect of genotype). There were no significant differences in the vVOR phases. These results indicated that there was a functional deficit in the semicircular canal of *Slitrk6*-KO mice.

We also performed behavioral tests related to vestibular functions, such as swimming, contact righting, and suspension [15]. In the suspension test, we did not see the trunk curling posture that is typically found in mice with impaired vestibular function [15] (data not shown). Swimming and contact righting did not show clear differences between the two genotypes (data not shown). In addition, *Slitrk6*-KO mice displayed a comparable performance to that of WT mice in the rota-rod test (Fig. 2D), which partly reflect vestibular function. These results suggested that the vestibular functional deficit in *Slitrk6*-KO mice is mild and selective for the posterior semicircular canal system.

Adaptive responses to environmental change are altered in *Slitrk6*-KO mice

In addition to inner ear–related abnormalities in *Slitrk6*-KO mice, novel phenotypes became clear based on their performance in a battery of behavioral tests (Table 1). First, we noticed altered activities of *Slitrk6*-KO mice in the home cage (Fig. 3). The activity level during the early dark phase tended to be lower (20:00–01:00, $P = 0.11$; 23:00–01:00, $P = 0.068$) and that during the beginning of the light phase was significantly higher (08:00–09:00, $P = 0.045$) than activity levels of the WT mice.

In an open field (OF) test with a 15-min observation period, the *Slitrk6*-KO mice showed less locomotor activity (Fig. 4A), although the difference was limited to the first 5 min (Fig. 4A; $P = 0.0023$). Furthermore, the percentage of time the *Slitrk6*-KO mice remained in the center area was significantly longer than the WT only in the first 5 min (Fig. 4B; $P = 0.0082$, Mann-Whitney's *U*-test). The abnormalities only in the early phase were thought to reflect some altered adaptive responses to the novel environment.

We also noted altered responses to a novel environment in the hole-board (HB) test, which was carried out for 5 min in a box that was the same size as the OF box. However, the HB box differed from the OF box in terms of color, brightness, and the presence of four holes on its floor. The total duration of head dipping into the holes by *Slitrk6*-KO mice was more than twice that of WT (Fig. 4D; $P = 0.046$). In addition, the latency to the first head dip was significantly shorter than that in the WT (Fig. 4E; $P = 0.028$).

Because *Slitrk6*-KO mice showed altered spontaneous activities in the three different contexts (home cage, OF box, and HB box), we evaluated whether these behavioral abnormalities were caused by elevated anxiety in a novel environment. We therefore performed the elevated plus maze test and light–dark box test, which are commonly used in neurobiological anxiety research. In these tests, however, we did not find any obvious differences between WT and *Slitrk6*-KO mice (Fig. 5). These results indicated that alterations of spontaneous activity in the home cage, OF, and HB tests are due to cognitive dysfunction in the *Slitrk6*-KO mice, rather than elevated anxiety.

The Morris water maze test, fear-conditioning test, forced swimming test, social interaction tests, tail flick test, and hot plate test did not show any abnormalities in the *Slitrk6*-KO mice as compared to the WT (Table 1).

Discussion

The *Slitrk6*-KO mouse is a novel animal model of sensorineural deafness

ABRs and ASRs indicated that there is an impaired auditory function in *Slitrk6*-KO mice. A mild (ca. 20-dB) elevation of the sound intensity threshold was observed for 8- and 16-kHz sound stimuli, resulting in a strong decrement of the ABR first wave (peak I). The results suggest that the reduction of peak I to the 80-dB stimulus is related to both the *Slitrk6* loss-of-function and the impaired auditory function. Although the precise origins of ABR waves are not yet well defined, it is generally agreed that the first wave represents activities of the auditory nerve and the late waves represent neural transmission within the central auditory circuit [16]. Our previous study revealed that during embryonic development of *Slitrk6*-KO mice the number of axon projection from the spiral ganglion to cochlear hair and the number of the spiral ganglion neurons were lower than seen in WT mice [5]. The total cell number in the spiral ganglion of *Slitrk6*-KO mice was one half that in WT, and the decreased number of the projection was clearly observed as late as 4 weeks after birth. Therefore, it is likely that the reduction of peak I may reflect these morphological differences in the inner ear neural circuit of *Slitrk6*-KO mice.

It is interesting that elevation of the sound intensity threshold was not observed for the 24-kHz sound stimulus. The frequency-selective sensitivity loss might not be fully explained by the innervation defects in the inner ear, considering that the projection impairment was generally observed from the basal to apical region of the cochlea. It is possible that some mechanism compensates for the desensitization to 24-kHz sounds. The enigmatic peak III increment might reflect such a process.

Many genes are associated with hearing impairment in mice [17,18], and 44 of them have been linked to human hereditary hearing loss [17]. Our findings indicate that *Slitrk6*-KO mice could be a novel model of sensorineural deafness. According to the current hereditary hearing loss database (http://hereditaryhearingloss.org), the nearest neighboring gene related to hearing impairment is an autosomal dominant nonsyndromic gene (DFNA 33, 13q34-qter) [19] approximately 27 Mb apart from *SLITRK6* (13q31.2). Thus, the involvement of functional deficits in *SLITRK6* in human hereditary hearing impairment awaits further investigation. Furthermore, *Slitrk6* inner ear abnormalities are known to involve altered neurotrophin-signaling [5]. NT-3 delivery has been attempted in model animals [20–22] with the aim of clinical treatment of hearing impairment, and it would be beneficial to

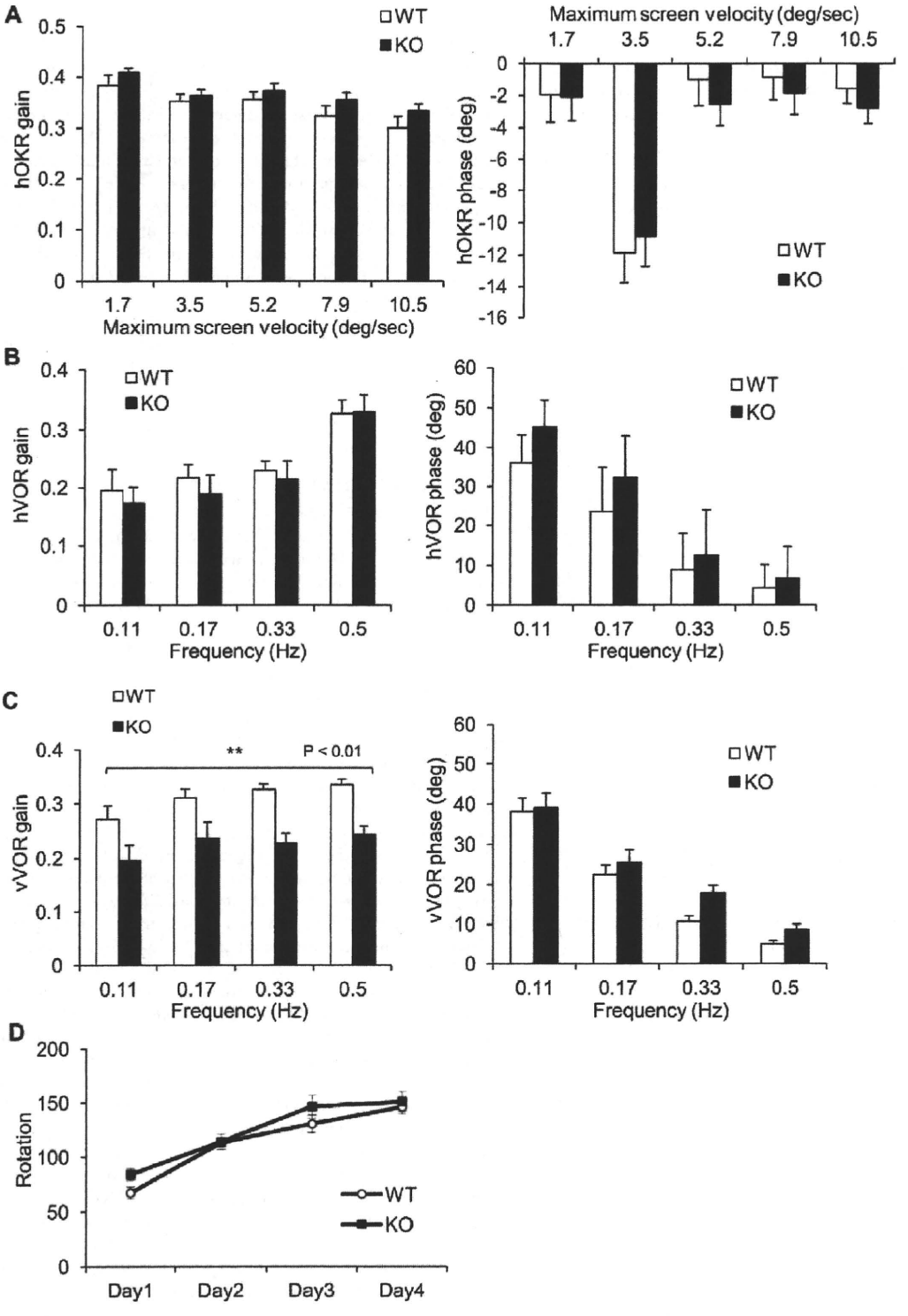

Figure 2. Vestibular function anomaly in *Slitrk6*-KO mice. (A) Dynamic characteristics of horizontal optokinetic response (hOKR) of WT ($n = 9$) and *Slitrk6*-KO ($n = 9$) mice. (B) Horizontal vestibulo-ocular reflex (hVOR). There were no differences in gains (left) or phases (right) between WT ($n = 9$) and KO ($n = 9$) in hVOR or hOKR. (C) Vertical vestibulo-ocular reflex (vVOR) of WT ($n = 8$) and *Slitrk6*-KO mice ($n = 6$). Gains of vVOR (left) of the *Slitrk6*-KO mice were significantly smaller than those of WT. (D) Rota- rod test. Rotation indicates the speed of rotation (rpm) at which the mice fell off or revolved around the rod. The values were comparable between WT ($n = 12$) and *Slitrk6*-KO ($n = 8$) mice, suggesting that there were no strong deficits of balancing function in *Slitrk6*-KO mice. Values are mean ± standard error of the mean.
doi:10.1371/journal.pone.0016497.g002

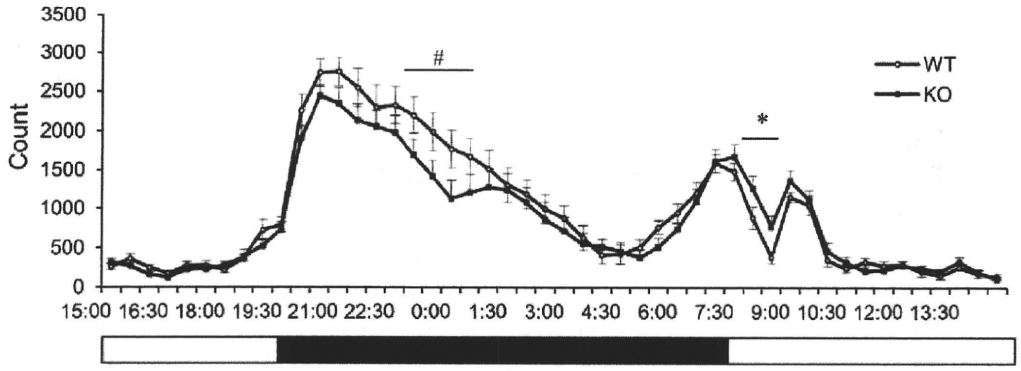

Figure 3. Spontaneous activity in home cage. Each vertical bar represents standard error of the mean. $^{\#}P=0.068$; $^{*}P<0.05$. WT, $n=10$; KO, $n=10$. Below the graph, open and black bars indicate light phase (08:00–20:00) and dark phase (20:00–08:00), respectively.
doi:10.1371/journal.pone.0016497.g003

further clarify the mechanism of *Slitrk6* action in development of the inner ear and auditory signal processing.

Vestibular function abnormalities in *Slitrk6*-KO mice

Slitrk6-KO mice showed moderate deficit in the gain of vVOR, but not in hVOR. Based on the orientations of mouse semicircular canals [23], horizontal semicircular canals are selectively stimulated in the test of hVOR, whereas the anterior and posterior semicircular canals are equally stimulated in the test of vVOR in our assay system. The involvement of otolith in the head rotation used in our vVOR test was small, as the effect of gravity was minimal in the head rotation in nose-up position perpendicular to the earth axis. On the other hand, we previously showed that the neural projection to posterior crista, which develops to posterior semicircular canal, was often lost in *Slitrk6*-KO mice (78.3% at E13.5 [$n=83$], 85.7% at E15.5 [$n=28$], and 90.3% after P14 [$n=62$]), but those to the anterior and horizontal canal cristae and otolith organs remained intact [5]. Thus, the defect of VOR (normal hVOR and impaired vVOR) is consistent with the anomaly of vestibular nerve projection (intact innervation of anterior and horizontal cristae and decreased innervation of posterior crista) in *Slitrk6*-KO mice. Concurrently, the VOR results suggest that function of *Slitrk6*-KO horizontal canal is not obviously impaired, indistinguishable from those of WT. However, the functional and structural properties of the remained inner ear neural circuits of *Slitrk6*-KO should be more carefully examined because embryonic *Slitrk6* expression broadly occurs in the inner ear sensory epithelia [5].

Many mutant mice with vestibular function abnormalities are listed in the current mouse genome informatics database (http://www.informatics.jax.org/). However, we did not find any mice with vertical-direction limited VOR abnormalities. In this regard, the vestibular dysfunction in *Slitrk6*-KO mice is unique. Together with the selective innervation defects to the posterior crista, *Slitrk6*-KO mice could serve as a useful model to study the role of the semicircular canal in vestibular function.

Although the vestibular function alteration was clear in the vVOR, it is unclear how the other behavioral phenotypes in *Slitrk6*-KO mice reflect the altered vestibular function. For example, *Slitrk6*-KO mice showed a significant decrement in the immobility time of the tail suspension test (Table 1). This alteration could indicate the absence of a normal vestibular response for vertical head movement. However, even if this is the case, the overall vestibular function deficit appears to be mild and selective. The vestibular innervation defects in the posterior canal may be partially compensated by the anterior semicircular canal and possibly the otolith organs, which also sense vertical head movements.

In humans, a posterior semicircular canal dysfunction is related to benign paroxysmal positional vertigo, in which displaced otoconia are thought to enter a semicircular canal, usually in the posterior one [24,25]. Although this is a disorder of late onset (mean onset 54 years old) [24], there are pediatric patients with balance and vestibular disorders [26,27]. Considering that significant associations exist between sensorineural hearing loss and balance disorders [26], it is possible that *SLITRK6* is involved in some pathophysiological processes of pediatric vestibular disorders.

Cognitive dysfunction of *Slitrk6*-KO mice

This study revealed novel behavioral phenotypes of *Slitrk6*-KO mice (Table 1). Among them, the abnormalities revealed by the OF and HB tests may reflect similar aspects of altered higher brain function in *Slitrk6*-KO mice. In both tests, the abnormalities appeared soon (within 5 min) after entry into the test boxes. Therefore, we assume that the novel environments induced the differential behaviors. Our findings clearly indicated a neurological basis for these behavioral abnormalities, which appeared to reflect increased attention to the environment and emotional responses similar to "restlessness" or "confusion."

It is tempting to correlate these behavioral abnormalities with the role of *Slitrk6* in the thalamus, where its expression is clearly demarcated among regions of the central nervous system [1,4,6]. If we assume that the thalamic expression is significant, some sensory information processing during adaptive behaviors may be dysfunctional in *Slitrk6*-KO mice, considering the many roles played by the thalamus in relaying and modulating sensory signals [28–30]. Future studies should examine whether *Slitrk6* loss-of-function impairs the development or the function of the thalamic neural circuit. Clarification of the molecular function of *Slitrk6* will contribute to a better understanding of the higher function of the mammalian brain.

Materials and Methods

Animals

Animal experiments were approved by the Animal Experiment Committee of the RIKEN Brain Science Institute (approval no. H18-2B032), and the mice were maintained at the institute's

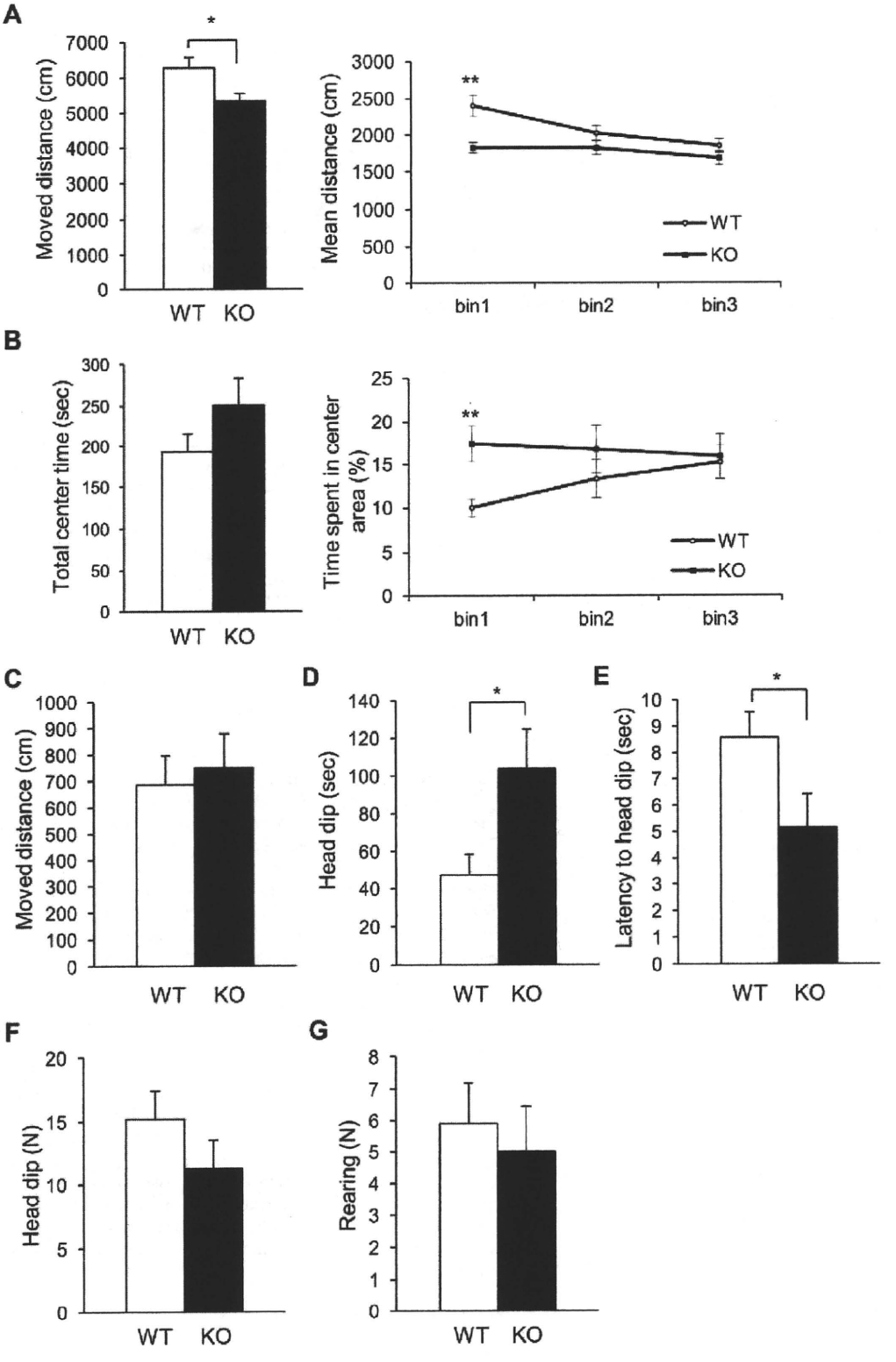

Figure 4. Altered adaptive responses to a novel environment in *Slitrk6*-KO mice. (A, B) Open field test. (A) The total distance moved was less in *Slitrk6*-KO than in WT mice (left). The distance moved in the first 5 min of the test was significantly lower in *Slitrk6*-KO mice (right). (B) In *Slitrk6*-KO mice, the total time spent in the center area was greater than that of the WT (left) and was significantly increased in the first 5 min of the test

(right). (C–G) Hole-board test. There were no significant differences in distance moved (C), number of rearing episodes (D), and number of head dips (E) between *Slitrk6*-KO and WT mice. Duration per head dip was significantly decreased in *Slitrk6*-KO mice (F). Latency time to head dip was significantly decreased in KO mice (G). Values are mean ± standard error of the mean. *$P<0.05$, **$P<0.01$ for Mann-Whitney's *U*-test (B, center area data) or Student's *t*-test (others). WT, $n=10$; KO, $n=10$.
doi:10.1371/journal.pone.0016497.g004

Research Resource Center. The mice were kept on a 12-h light–dark cycle, with the dark cycle occurring from 20:00 to 08:00. All the testing described here was performed with adult male mice. The behavioral tests were started when the mice were 12 weeks old and completed before they reached the age of 16 weeks. In total, 45 pairs of WT and KO mice were used in this study.

Auditory brainstem response

For the measurement of ABRs, mice were anesthetized with an intraperitoneal injection of 60 mg/kg sodium pentobarbital (Nembutal, Dainippon Pharmaceutical Co., Ltd., Osaka, Japan), and needle electrodes were inserted at the vertex and pinna with a ground near the tail. ABRs were evoked with 4-ms tone pips at 40 per second with a 0.4-ms cosine squared rise–fall envelope and alternating in polarity to remove frequency-following responses. The voltage difference between the pinna and vertex was amplified (10,000×), filtered, digitized at 100 kHz, and averaged across 512 presentations. The sound level was decreased in 10-dB steps from an 80-dB sound pressure level. The threshold, amplitude, and latency of responses were defined by visual inspection of stacked waveforms.

Auditory startle response

In this test, each mouse was put into a small cage (30 or 35 mm diameter, 12 cm long) that was set on a sensor block within a sound-proof chamber (60×50×67 cm [height]). A dim light was equipped on the ceiling of the sound-proof chamber (10 lux at the center of the sensor block), and a 65-dB white noise was presented

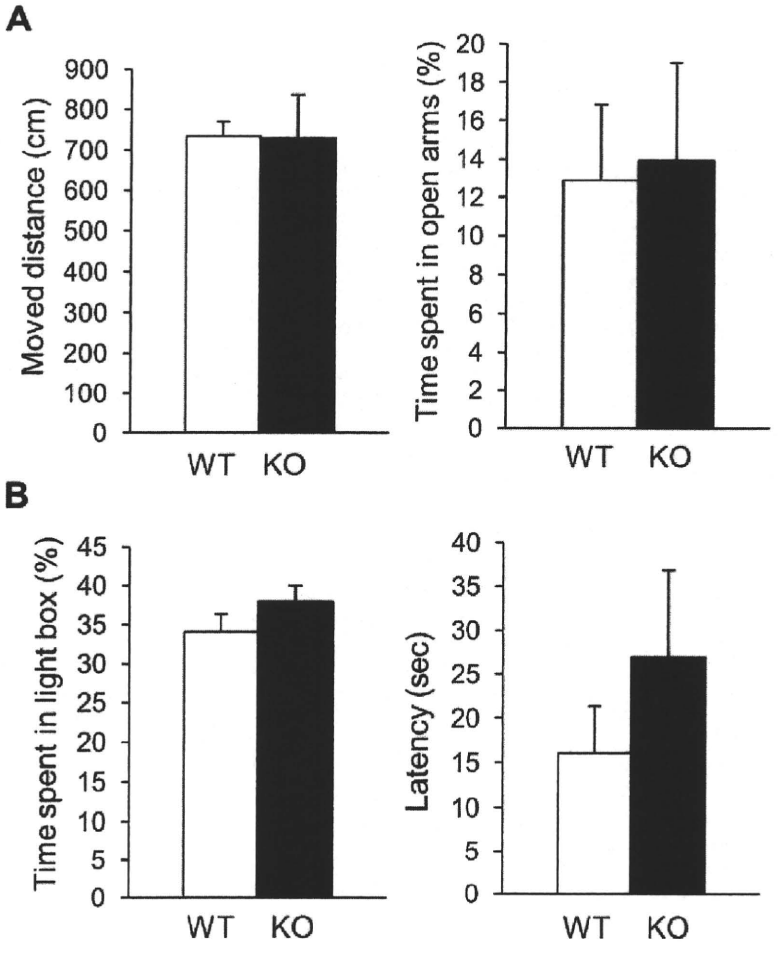

Figure 5. Normal anxiety level of *Slitrk6*-KO mice. (A) Elevated plus maze test. There was no difference between the genotypes in terms of distance traveled (left) or time spent in open arms (right). (B) Light–dark box test. Latency to the first entry into the dark box (left) and time spent in the light box (right) were not significantly different between WT and *Slitrk6*-KO mice. Values are mean ± standard error of the mean. WT, $n=10$; KO, $n=10$.
doi:10.1371/journal.pone.0016497.g005

as background noise. In the ASR test, each mouse was acclimatized to the experimental condition for 5 min, then the experimental session began. In the first session, a 120-dB startle stimulus (40 ms) was presented to the mouse 10 times at random intertrial intervals (10–20 s). In the second session, the startle response to stimuli at various intensities was assessed. Five times of 70 to 120 dB (70, 75, 80, 85, 90, 95, 100, 110, 120 dB) white noise stimuli (40 ms) were presented in quasi-random order and random inter-trial intervals (10–20 sec). In the prepulse inhibition session, the mouse experienced five types of trials: (1) no stimulus; (2) startle stimulus (120 dB, 40 ms) only; (3) 70-dB prepulse (20 ms, lead time 100 ms) and 120-dB pulse; (4) 75-dB prepulse (20 ms, lead time 100 ms) and120-dB pulse; and (5) 80-dB prepulse (20 ms, lead time 100 ms) and 120-dB pulse. Each trial was repeated 10 times in quasi-random order at random intertrial intervals (10–20 s). In the final session, again a 120-dB startle stimulus (40 ms) was presented to the mouse 10 times at random intertrial intervals (10–20 s). The total duration of an ASR test was about 35 to 40 min. After each trial, holding chambers were washed with tap water, wiped with a paper towel, and dried. Apparatuses and software for data analysis used were commercially available ones (Mouse Startle, O'Hara, Tokyo, Japan).

Vestibulo-ocular reflex and optokinetic response eye movements

Eye movement was measured by the infrared TV method as described previously [31,32]. Under isofluorane (Escain, Mylan-Japan, Tokyo, Japan) anesthesia and aseptic conditions, a platform for head fixation was made on the mouse cranial bone using synthetic resin (Superbond C &B, Sun Medical, Tokyo, Japan) and one 15-mm stainless bolt. Two days after surgery, a mouse was mounted on the turntable surrounded by a checked-pattern (check size, 4°) screen (diameter, 60 cm; height, 60 cm), with the head fixed and the body loosely restrained in a plastic cylinder. The horizontal and vertical vestibulo-ocular reflexes (hVOR and vVOR, respectively) and horizontal optokinetic response (hOKR) eye movements were measured. The hVOR was tested in the dark by sinusoidal turntable oscillation at a frequency of 0.11–0.50 Hz and peak-to-peak amplitude of 10° on the plane parallel to the bilateral horizontal semicircular canals. The hOKR was tested in the light with sinusoidal screen oscillation at a frequency of 0.11–0.33 Hz and peak-to-peak amplitude of 10–20° (maximum screen velocity, 3.5–10.5°/s) on the same plane. The vVOR was tested in the dark with turntable oscillation at a frequency of 0.11–0.5 Hz and peak-to-peak amplitude of 10° on the plane perpendicular to the plane of the bilateral horizontal semicircular canals. During the test of vVOR, the mouse laid on its back in the plastic cylinder with the head-up position on the turntable [33]. More than 10 cycles of the evoked horizontal (hVOR and hOKR) or vertical (vVOR) eye movements free from artifacts due to blinks and saccades were averaged, and the mean amplitude and phase were calculated by a modified Fourier analysis [34]. A gain of the eye movement was defined as the ratio of the peak-to-peak amplitude of eye movements to that of the turntable or screen oscillation. The phase was defined as 0° when the peak of the eye movement was opposite to the peak of turntable oscillation in the hVOR and vVOR and when the peak of the eye movement matched the screen oscillation in the hOKR.

Rota-rod test

A mouse was placed on a rotating rod (O'Hara) and the time it was able to maintain its balance walking on top of the rod was measured. The speed of rotation was 4 rpm on day 1, and the speed was accelerated from 4 to 40 rpm over a 4-min period and then maintained at 40 rpm for another 1 min on days 2 to 5. Mice were tested in one trial for 2 min on day 1 and in four trials with a maximum time of 300 s (intertrial intervals were 20–30 s) on days 2 to 5. The time between placement and falling off or revolving around the rod was recorded manually.

Home cage activity

Spontaneous activity of each mouse in its home cage was measured using a 24-channel ABsystem 4.0 (Neuroscience, Tokyo, Japan). Cages were individually set into the stainless steel compartments of a negative breeding rack (JCL, Tokyo, Japan). An infrared sensor was equipped on the ceiling of each compartment and it detected movements of the mice. Home cage activity was measured for 1 week, starting from the afternoon of the day mice were transferred to the behavioral laboratory (day 1). Only data from days 2 to 8 were statistically analyzed. After termination of the home cage activity measurements, cages and bedding materials were changed and the mice were maintained in a micro-isolation rack (Allentown, PA, USA) throughout the behavioral screening.

Hole-board test

For this test, an OF system made of gray plastic (50×50×40 cm [height]) with four equally separated holes (3 cm diameter, each with an infrared sensor) on the floor was used (model ST-1/WII, Muromachi-kikai, Tokyo, Japan). The field was illuminated by fluorescent light (180 lux at the center of the field), and the level of background noise was approximately 50 dB. The behavior of each mouse was monitored by a CCD camera (placed about 1.5 m above the field). In the HB test, a mouse was introduced into the center of the field and allowed to explore freely for 5 min. Total moving time (s), distance traveled (cm), latency for head dipping (s), number of head dips, duration of head dipping (s), duration of rearing (s), and number of rearing episodes were measured as indices. Data were collected and analyzed using CompACT VAS system (Muromachi-kikai).

Open field, elevated plus maze, and light–dark box tests

Open field, elevated plus maze, and light–dark box tests were performed as described previously [35].

Statistical analyses

Statistical analyses were conducted using the SPSS statistical package (ver. 16.0, SPSS Japan Inc., Tokyo, Japan). Parametric data were analyzed by Student's *t*-test, and nonparametric data were analyzed by Mann-Whitney's *U*-test. Reported *P* values refer to Student's *t*-test unless otherwise noted. Effects of factors were analyzed by one-way ANOVA, two-way ANOVA with post hoc tests, and generalized linear model. Differences were defined as statistically significant when $P<0.05$.

Acknowledgments

We thank Hiromichi Goto (RIKEN Brain Science Institute) for teaching us how to perform the ABR measurement, and Azel Zine (University of Montpellier I) for valuable discussions.

Author Contributions

Conceived and designed the experiments: YM KK SN JA. Performed the experiments: YM KK TO KY NT SN. Analyzed the data: YM KK TO KY NT SN JA. Wrote the paper: YM KK KY SN JA.